# AN ABSTRACT OF THE THESIS OF

Matthew Mauch for the degree of Master of Science in Ocean, Earth, and Atmospheric Science presented on September 15, 2017.

Title: Coastal Ocean Variability Inferred from High Resolution Models: two case studies.

Abstract approved:

_____

Alexander L. Kurapov

In this thesis, high resolution ocean models are used to evaluate and forecast coastal ocean variability in two different applications.

In the first study, the 2-km resolution ocean circulation model for the Eastern Bering Sea is utilized to understand whether slope-interior exchange along the path of the Aleutian North Slope Current (ANSC) helps maintain the subsurface temperature maximum on the isopycnal surface 26.8 kg $m^{-3}$, approximately 300-400 m deep. The simulation period is June-October of 2009. At the abovementioned isopycnal surface, the model shows the warmer pattern extending westward along the southern slope of the Aleutian Islands and then eastward along the northern slope as the season progresses. The direct exchange from the south to the north through Amukta Pass on this isopycnal surface is very limited. The model does not exhibit vigorous eddy shedding along the ANSC. However, there are several topographic features where the warm slope current separates into the basin, particularly at 178˚ W (just east of Amchitka Pass) and 174˚ W (Atka Island). Currents on the 26.8 kg $m^{-3}$ isopycnal surface are too slow to account for the warming pattern along the ANSC reaching the

Bering Canyon and the Bering Slope Current. The warming can be explained as a combination of faster advection of warmer waters above and downward vertical turbulent transport due to intensive tides. This hypothesis is confirmed by the heat equation term balance analysis and two-dimensional Lagrangian particle tracking on the 26.8 kg $m^{-3}$ surface and a shallower, 26.4 kg $m^{-3}$ surface.

In the second study, a team of four graduate students, including two ocean modelers, a cartographer, and a social scientist, work together as part of the National Science Foundation Research Trainee (NRT) program to develop new products based on ocean forecasts, quantify their uncertainty and communicate this knowledge to commercial fishermen. A 2-km resolution ocean prediction system for the Oregon and Washington coasts produces three-day forecasts of surface velocity, temperature, and salinity. Based on the social scientist's communications with the commercial fishermen on their perceptions of risk and uncertainty, uncertainty in the surface current forecast is quantified by calculating the root mean square error of the forecast with high frequency radar observations for each forecast horizon. This calculation reveals that the model performs better in the northern portion of the domain where high frequency radar observations are available, with a noticeable source of error being near the Columbia River Estuary. Additionally, the depth of the thermocline is calculated with two different methods: as a depth at which the temperature is 2˚F less than the surface temperature (a definition provided by the commercial fishermen) and as a depth of the maximum buoyancy frequency squared.

Overall, the two parts of our thesis study complement each other showing that coastal ocean models can be used both for basic oceanographic research and for operational prediction.

# Coast Ocean Variability Inferred from High Resolution Models: two case studies

by
Matthew Mauch

A THESIS

submitted to

Oregon State University

in partial fulfillment of
the requirements for the
degree of

Master of Science

Presented September 15, 2017
Commencement June 2018

Master of Science thesis of Matthew Mauch presented on September 15, 2017

APPROVED:

Major Professor, representing Ocean, Earth, and Atmospheric Science

Dean of the College of Earth, Ocean, and Atmospheric Science

Dean of the Graduate School

I understand that my thesis will become part of the permanent collection of Oregon State University libraries. My signature below authorizes release of my thesis to any reader upon request.

Matthew Mauch, Author

# TABLE OF CONTENTS

Page

1 Introduction..... 1

2 Connectivity of the Aleutian North Slope Current and Bering Sea basin waters at the level of the subsurface temperature maximum: a modeling study ..... 3

2.1 Introduction .....3

2.2 Model Setup .....5

2.3 Results .....7

2.3.1 Mean Stratification and flow features in the ANSC .....7

2.3.2 Temperature variability and transports on the isopycnal surfaces…9

2.3.3 Heat equation term balance analysis .....12

2.3.4 Locations of intensified warmer water separation from ANSC to the deep basin.....15

2.3.5 Backward particle tracking .....17

2.4 Summary .....18

2.5 References .....20

Figures .....24

3 Minor Chapter: Forecast product and uncertainty quantification off the Oregon/Washington Coast .....37

3.1 Introduction .....37

3.2 Approach .....40

3.2.1 Transdisciplinary Process .....40

3.2.2 Defining Uncertainty .....41

3.2.3 Communicating Uncertainty in Ocean Forecasts .....42

3.3 Model Setup .....43

TABLE OF CONTENTS (Continued)

Page

3.4 Results …….....…...45

3.4.1 New forecast products ……...……45

3.4.2 Uncertainty Quantification ……...……46

3.5 Summary ...…….....48

3.6 References …….....49

Figures …..…...…….....52

Bibliography ……...60

# LIST OF FIGURES

Figure Page

Figure 1. ……24

Figure 2. ……...25

Figure 3. ……...26

Figure 4. ……..……27

Figure 5. ……...……..28

Figure 6. ……29

Figure 7. ……30

Figure 8. ……31

Figure 9. ……..……32

Figure 10. ……33

Figure 11. ……34

Figure 12. ……35

Figure 13. ……36

Figure 14. ……52

Figure 15. ……53

Figure 16. ……54

Figure 17. ……55

Figure 18. ……56

Figure 19. ……57

Figure 20. ……58

Figure 21. ……59

## 1. Introduction.

This thesis has two chapters. The first is in fulfillment of the requirement for the Master of Science Degree in Earth, Ocean, and Atmospheric Science and is dealing with the problem of flows around Aleutian Islands and in the Bering Sea. The second chapter is part of the requirement for the minor degree in Risk and Uncertainty Quantification in Marine Science supported by the National Science Foundation Research Traineeship (NRT) program. This chapter describes my contribution to the NRT student team effort and is focused on new statistics and products for the real-time forecast ocean model off Oregon. Although the two chapters consider different geographic domains and physical regimes, the unifying theme is the demonstration of the utility of high-resolution ocean circulation models for basic process studies (as in Chapter 1) and operational prediction (as in Chapter 2). Both the Eastern Bering Sea and the U.S West Coast feature unique dynamics and important biological interactions supporting ecosystems and fisheries in their respective areas. Regional ocean modeling provides a powerful tool to scientists and stakeholders, allowing the evaluation of physical interactions and forecasting of valuable information.

In Chapter 1, a high-resolution model spanning the Eastern Bering Sea is utilized to investigate patterns of slope-ocean interior momentum, material, and heat exchange and help explain the sources of the subsurface temperature maximum observed in the region. In this part, our studies include the term balance analysis of the temperature equation and forward and backward Lagrangian particle tracking on selected subsurface levels of constant density.

Chapter 2 explains some details of the NRT project that has involved the collaboration of four graduate students, each residing in their own discipline, to attack a single problem. The project aims at development of new products that add value to the outputs of the Oregon-Washington coastal ocean forecast system run at OSU. The forecast model was used to develop a method of uncertainty quantification and new forecast products for commercial fishermen, the primary users of the forecasts. The interests and necessities of the commercial fishermen guide the analyses provided in this project.

The introductions, model setups, results, and conclusions of each of these projects will be discussed separately, in their entirety, beginning with the Eastern Bering Sea model and ending with the U.S. West Coast model.

## 2. Connectivity of the Aleutian North Slope Current and Bering Sea basin waters at the level of the subsurface temperature maximum: a modeling study

### 2.1 Introduction.

The Eastern Bering Sea is a unique region featuring both complicated dynamics and important biological interactions that support one of the richest and most diverse ecosystems in the world [*Hunt et al.*, 2008]. It is bounded by Alaska to the east, the Aleutian Islands chain to the south, and the Russian Chukotka coast to the northwest (Figure 1). The mean, large-scale circulation in the Bering Sea region is defined by the Alaskan Stream carrying relatively warmer Pacific waters westward along the southern slope of the Aleutian Island chain [*Favorite*, 1974], a cyclonic gyre circulation in the Bering Sea deep basin [*Panteleev et al.*, 2012], and slow and diffused mass and heat transport over the shelf toward the Bering Strait [*Danielson et al.*, 2011]. Currents from the North Pacific connect to the Eastern Bering Sea through the Aleutian Island passes [*Stabeno et al.*, 2005; *Clement Kinney and Maslowski*, 2012]. The Aleutian North Slope Current (ANSC) flows eastward along the northern slope of the Aleutian Islands. The water properties of this fast (observed as high as 0.8 m $s^{-1}$ [*Stabeno et al.*, 2009]) and narrow (~20 km) current are heavily influenced by the flow through the Aleutian Passes [*Reed and Stabeno*, 1999] and local tidally driven mixing. Tidal flows are strong around the Aleutian Islands providing energy for mixing into the passes and along the island chain slope [*Kowalik*, 1999; *Foreman et al.*, 2006; *Nakamura et al.*, 2010]. In particular, diurnal tides are near resonance along portions of the Aleutian North Slope. Tidally averaged transports along the slopes and through the passes are modulated approximately at the 14-day period, correlated with periods of spring and neap tide for the combination of the diurnal $K_1$ and $O_1$ tidal constituents [*Stabeno et al.*, 2005; *Durski et al.*, 2015].

The ANSC carries the Pacific water to the Bering Canyon (167˚ W) before turning to the northwest and flowing along the shelf break as the Bering Slope Current (BSC). Exchange between the deep basin, slope, and the 500-km-wide shelf is controlled by the wind-driven Ekman transport [*Danielson et al.*, 2011, 2012, 2014] and large-scale eddies that are more abundant in the deep basin in summer than in winter [*Ladd*, 2014].

A temperature inversion (i.e., a layer of relatively warmer temperature) at depths of ~150-300 m has been observed in a section from Amchitka Pass through the Bering Sea basin to Zhemchug Canyon [*Roden*, 1995]. *Stabeno et al.* [2009] also observed a weak subsurface temperature inversion layer between 200-400 m further east in sections across the ANSC and BSC close to the Bering Canyon. The subsurface temperature maximum is most pronounced in winter, when the surface layer is cooled, and it is still detectable in summer. Johnson et al. [2004] observed this subsurface maximum in the float profiles and noted that it generally resides on the isopycnal surface $\sigma_\theta$ =26.8 kg m$^{-3}$ (where $\sigma_\theta = \rho - 1000$ [kg m$^{-3}$] and $\rho$ is the potential density referenced to the surface). *Stabeno et al.* [2009] hypothesized that the source waters for this layer should be found in Amukta Pass. It is deep enough (~450 m at its deepest) such that relatively warmer subsurface Pacific waters can flow in and it is close enough (about 200 km) to the Bering Canyon region. Additionally, waters in Amukta Pass and in the subsurface maximum layer in the Bering Canyon shared similar water properties. As will be shown in this manuscript, a high-resolution model can provide a more detailed view of the exchange of ANSC and interior basin waters at this subsurface layer and point to several locations along the rim of the basin where slope-interior flow and heat exchange take place.

Several numerical studies of the eastern Bering Sea have been undertaken (e.g., *Clement et al.*, 2005; *Clement Kinney et al.*, 2009; *Ezer and Oey*, 2010; *Hu and Wang*, 2010; *Zhang et al.*, 2010; *Danielson et al.*, 2011; *Clement Kinney and Maslowski*, 2012; *Panteleev et al.*, 2012; *Li et al.,* 2014), with focus on the mean circulation and seasonal and interannual variability in the volume transports, heat fluxes, ice extent, ice concentration, and ice mass. However, none of these attempted to model the entire eastern Bering Sea region at a resolution below 4 km, nor did they focus on the ANSC structure. Here we use the 2-km resolution model developed by Durski et al. [2015] (Section 2) to find the aforementioned subsurface temperature maximum layer, and to understand the details of the transport and mixing within the ANSC and their contribution to the temperature balance at $\sigma_\theta$ =26.8 kg m$^{-3}$ (Section 3). In particular, we will demonstrate that Amukta Pass is not the only region where intensified separation of relatively warmer ANSC waters into the basin at the level of the subsurface temperature maximum occurs. Section 4 presents a summary.

**2.2 Model Setup.**

The model application utilized here [*Durski et al.*, 2015] is based on the Regional Ocean Modeling System (ROMS, www.myroms.org) which is a non-linear, three-dimensional, free surface, hydrostatic, Boussinesq ocean model. It uses terrain following vertical coordinates and advanced numerics [*Shchepetkin and McWilliams*, 2003, 2005]. The Mellor-Yamada level 2.5 closure is used to parameterize vertical mixing [*Mellor and Yamada*, 1982] with modifications from *Kantha and Clayson* [1994]. Momentum dissipation along s-coordinate surfaces is handled as a harmonic viscosity with a coefficient of 5 m$^2$ s$^{-1}$. The COARE algorithm [*Fairall et al.*, 2003] as implemented in ROMS is used to parameterize surface fluxes. Explicit horizontal

diffusivity for temperature and salinity is set to zero. A roughness length of 0.02 m is used to parameterize bottom stress quadratically.

The model extends from 182.75˚ W to 154˚ W and 50˚ N to 66.4˚ N (Figure 1) with a horizontal resolution of about 2 km and 45 vertical layers. The vertical resolution is higher near the surface and bottom. The bathymetry has been interpolated from the Alaska Region Digital Elevation Model (ARDEM, http://mather.sfos.uaf.edu/~seth/bathy). Some smoothing was applied near the Aleutian Islands and along the Bering Sea slope where necessary to reduce terrain-following-coordinate pressure gradient errors. Additionally, the bathymetry is made to smoothly match the model providing boundary conditions at all model edges.

Initial conditions are obtained by combining fields from the 1/12˚ resolution Navy Hybrid Coordinate Ocean model (HYCOM [*Chassignet et al.*, 2007], http://www.hycom.org) with a BESTMAS regional simulation [*Zhang et al.*, 2010] for June 1, 2009. HYCOM provided an adequate initialization for the Bering Sea Basin and North Pacific, but failed to accurately represent the vertical temperature structure of the Bering Shelf in early June 2009. For this reason, the BESTMAS solution was used on the shelf and smoothly blended at the shelf break with the HYCOM fields.

Open boundary conditions for horizontal velocity, potential temperature, and salinity are provided by a combination of nudging (on a 3-day time scale for inflow) to HYCOM and Orlanski radiation. HYCOM provides instantaneous fields once a day; to reduce the effect of aliasing inertial motion and day-to-day noise, a 4-day low pass filter is applied to these fields. The turbulent kinetic energy equation uses an Orlanski radiation condition, but without nudging. A 50-km wide sponge of increased horizontal viscosity and diffusivity is placed at the western boundary of the model domain to reduce inaccurate boundary effects that would otherwise occur.

For sea surface height, a gravity-wave radiation condition is due to [*Chapman*, 1985] combined with the *Flather* [1976] condition for the barotropic velocity components. Tides are forced using four constituents ($K_1$, $O_1$, $M_2$, $S_2$) applied at the model boundaries with amplitudes and phases provided by the OSU tidal inversion global model (TPXO) [*Egbert and Erofeeva*, 2002].

Atmospheric forcing for the model is obtained from the North American Regional Reanalysis (NARR) [*Mesinger et al.*, 2006] with a 25% reduction in surface solar radiation due to the documented over-insolation of NARR at high latitudes during the summer [*Walsh et al.*, 2009]. The model simulation discussed below is run for an ice-free period of June 1 to October 31, 2009. This model application was developed and first tested by *Durski et al.* [2015] who demonstrated the model accuracy over the shelf and along the Aleutian Islands by comparing the model against satellite SST, Argo temperature and salinity profiles, and shelf moorings. The research showed advantages of the 2-km resolution that allowed the description of frontal variability around the Aleutians, corrugations of the cold pool front on the shelf, and internal tides over the edge of the Bering Sea shelf.

## 2.3 Results.

### *2.3.1 Mean stratification and flow features in ANSC*

To confirm the presence of the subsurface temperature maximum in our model, it is compared with temperature ($T$) and salinity ($S$) data from Argo floats in a $T$-$S$ diagram (Figure 2). Observations were from two different Argo floats: one recording 15 profiles from June 4 to October 22, 2009 and the other recording 5 profiles from June 10 to July 20, 2009, with each float taking a profile once every 10 days (see Figure 1, bottom, for the float tracks) [*Argo*, 2000].

The model $T$ and $S$ were interpolated to Argo locations and times. Both the model and Argo data show a decrease in temperature with increasing salinity for fresher waters, but for $S \approx$33.2-33.75 psu the temperature increases with increasing salinity before decreasing again with salinity for saltier water (Figure 2). The subsurface temperature maximum is found both in the model and observations at $\sigma_\theta =$26.8 kg m$^{-3}$ (bold contour in Figure 2), consistent with [*Johnson et al.*, 2004; *Stabeno et al.*, 2009]

To show the placement of the 26.8 kg m$^{-3}$ isopycnal surface with respect to the Aleutian slope currents, the monthly averaged zonal (approximately along-slope) current $u$ and $T$ are shown in the meridional section at 175˚ W across the island chain ridge, for the months of July, August, and September (Figure 3). In these sections, the monthly mean location of $\sigma_\theta =$26.8 kg m$^{-3}$ is plotted (solid line) along with ± 1 standard deviation (dashed lines). A weak temperature maximum is apparent north of the islands between depths of 300-400 m, close to where the selected isopycnal surface is placed. The strongly negative $u$ corresponds to the westward Alaskan Stream on the southern slope and the strongly positive $u$ corresponds to the eastward ANSC. On both slopes, the current is about 20 km wide. The ANSC strength increases as summer progresses. The currents are strongly baroclinic, in qualitative agreement with the mean density surfaces caving down toward the slopes. The temperature over the slopes is higher than at the same depths in the Pacific and Bering Sea Basins and it is increasing as the summer progresses. The term balance analysis below will confirm that both advection of the warmer temperature in the core of the slope jets and vertical mixing at the bottom of those cores contribute to this seasonal warming trend. $\sigma_\theta =$26.8 kg m$^{-3}$ is within the lower half of the slope currents on both sides. The standard deviation in the depth of this layer is largest close to the slope reaching almost 100 m. This variability is mostly diurnal tide-driven oscillations. It is

anticipated that such repeated 200-m up and downslope isopycnal excursions in proximity to the slope bottom boundary layer coincide with diapycnal mixing processes that change water properties in the lower half of the ANSC.

*2.3.2 Temperature variability and transports on the isopycnal surfaces*

To understand the dynamics, sources, and the structure of the subsurface maximum layer, model temperature $T_\sigma$ and horizontal velocity components were sampled on two different isopycnal layers: 26.8 kg m$^{-3}$ and the shallower 26.4 kg m$^{-3}$ (generally ~175 m above 26.8 kg m$^{-3}$). A series of maps of daily averaged $T_{26.8}$ (Figure 4), shown here for 1 July, 15 August, and 15 October, displays the seasonal progression of higher slope-water temperatures on this surface, along with slope-interior ocean exchange. From June through mid-August, the relatively warmer Gulf of Alaska water (provided in the model boundary conditions), extends westward along the southern slope. Little direct exchange occurs across Amukta Pass (172˚ W) given that $z_{26.8}$ is close to the maximum bathymetric depth in the pass. The westward flow of warmer water on $\sigma_{26.8}$ appears to continue uninterrupted as far as Amchitka Pass (180˚ W) where the pattern splits with some of the warmer water continuing west along the southern slope and the rest entering the pass. Contrary to our expectation, the warm pattern does not just turn around the eastern flank of Amchitka Pass but rather separates into a vast area around Semisopochnoi (Unyak) Island (52˚N, 180.5˚ W) and Bowers Ridge (53-55˚N, 180˚W). The warmer water from the southern slope gets entrained in large and long-lived eddies that can travel great distances into the Bering Basin, *e.g.*, as the one in Figure 4c, centered at 53.5˚N, 178˚W. Toward the second half of summer, a pattern of warmer water becomes apparent at the level of 26.8 kg m$^{-3}$ within the ANSC, progressing eastward and feeding into the Bering Canyon and farther along the BSC. Persistent separation of the warmer waters into the Bering Sea Basin is found at several points along the northern slope.

Looking at a 4-month animation of $T_{26.8}$, using the full series of plots as in Figure 4, a viewer can be left with the impression that the emergence of the warmer waters in the ANSC is simply a result of advection of the source waters from the eastern Pacific boundary, along the south slope, wrapping around the eastern flank of Amchikta Pass and into the ANSC. However, analysis of alongslope transports suggests that advection on this isopycnal surface is not an effective mechanism to explain warming. To illustrate this, we do two-dimensional Lagrangian particle tracking on the isopycnal plane using instantaneous horizontal velocities sampled on $\sigma_\theta$ =26.8 kg m$^{-3}$ every 2 hours (Figure 5, top). In this analysis, we essentially assume that the particles are floats that have a buoyancy of 26.8 kg m$^{-3}$. 50 particles were released every 2 hours at start locations selected randomly south of Amukta Pass within the black box shown in the figure. The particles were released from 0 hr UTC on July 6, 2009 to 0 hr UTC on July 7, 2009, for a total of 650 particles. Each particle is tracked for 92 days and the particle locations are saved every hour.

Very few particles (~8%, red trajectories) were able to pass through Amukta Pass and many of them would recirculate around the islands. Only 4 particles made it to the Bering Slope. The majority of the particles (half-tone) stay in the Alaskan Stream and continue to flow westward where they either enter the Bering Sea through Amchitka Pass or continue flowing westward out of the model domain. Most particles that flow through Amchitka Pass get caught up in eddy activity near Bowers Ridge or recirculate around Semisopochnoi Island. Very few of these particles join the ANSC to continue eastward in this time period, and only one of these particles makes it back to the Amukta Pass area after traveling through Amchitka Pass. It is important to note that very few particles made it to or past the Bering Canyon, and of those that did, all travelled through Amukta Pass.

Lagrangian motion computed similarly on the shallower 26.4 kg $m^{-3}$ isopycnal surface shows a different pattern (Figure 5, bottom). Approximately 30% of particles are able to travel directly through Amukta Pass and continue eastward in the ANSC. About 12% of the particles released would flow through Amukta Pass and then recirculate through a different pass back into the Alaskan Stream or continuously recirculate, carried by tide-induced currents. Particles that continue westward in the Alaskan Stream either cross into the Bering Sea through the Aleutian passes resolved by the model or continue westward out of the domain. Similar to the 26.8 kg $m^{-3}$ isopycnal surface, many particles are caught in the eddies near Bowers Ridge or recirculate around Semisopochnoi Island. However, on this shallower level many more particles than on $\sigma_\theta$ =26.8 kg $m^{-3}$ join the ANSC and continue eastward. Of the particles that made it to the Bering Canyon (56˚N, 168˚W), some continue into the BSC where they are entrapped in the eddy activity near Pribilof Canyon. Some particles separate from BSC and continue toward the southwest, in qualitative agreement with the direction of the "westward countercurrent" discovered by *Ladd* [2014] based on satellite altimetry analysis. In the Lagrangian experiment on 26.4 kg $m^{-3}$, 7 particles reached positions in the BSC north of Pribilof Canyon.

To better see where the particles in each experiment could be found at any time, a spatial pdf of particle positions is made for the two isopycnals (Figure 6). Specifically, the model domain is broken down into 10x10 km grid cells, the number of particles in each grid cell at any time is registered, and this is normalized by the total number of particle locations saved at all the times. The pdf for $\sigma_\theta = 26.8$ kg $m^{-3}$ (Figure 6, top) confirms that most particles released just south of Amukta Pass only reach the entrance of Amchitka Pass. Very few join the ANSC.

The pdf for $\sigma_\theta = 26.4$ kg $m^{-3}$ (Figure 6, bottom) indicates the large number of particles travelling through Amukta Pass. Of these, the majority make it to the Bering Canyon area as a

part of the ANSC. Of the tracers not traveling through Amukta Pass, many go through Atka Pass (~175.5˚ W), and another large portion travels through Amchitka Pass.

*3.3 Heat equation term balance analysis*

Based on the particle tracking experiment described in sect. 3.2, it is apparent that along-slope advection of Gulf of Alaska water on $\sigma_\theta$ =26.8 kg m$^{-3}$ is too slow to account for warming along the ANSC and in the Bering Canyon. However, warmer waters on the 26.4 kg m$^{-3}$ surface are faster and are transported to ANSC more effectively, e.g., due to the leakage through Atka Pass discovered in the trajectory pdf (see Figure 6, bottom).

We hypothesize here that tidally induced mixing over the ANSC is important for providing downward turbulent transport of heat to the depths swept by the 26.8 kg m$^{-3}$ isopycnal over the tidal cycle. To investigate the potential contribution of the vertical mixing to warming at the level of $\sigma_\theta = 26.8$ kg m$^{-3}$, we analyze the terms in the temperature equation. The model was rerun for a period of June 1 to September 2, 2009 with additional output of the 2-hr averaged terms in the temperature equation. Schematically (e.g., using Cartesian coordinates for simplicity), the ROMS temperature equation is:

$$\frac{\partial(TH_z)}{\partial t} = -\left\{\frac{\partial(uTH_z)}{\partial x} + \frac{\partial(vTH_z)}{\partial y} + \frac{\partial(\Omega T)}{\partial s}\right\} + \left[\frac{\partial}{\partial s}\left(\frac{K_T}{H_z}\frac{\partial T}{\partial s}\right) + \frac{1}{C_p\rho}\frac{\partial R}{\partial s}\right], \qquad (1)$$

where $x$ and $y$ are the horizontal coordinates and $s$ is the vertical (nondimensional) coordinate; the $x$- and $y$-derivatives are taken along the terrain-following $s$-surfaces; $H_z = \partial z/\partial s$ is the instantaneous thickness of the computational cell that changes with time proportional to the total water depth changes; $\Omega$ is the vertical velocity component with respect to the moving $s$-surface; $K_T$ is the vertical eddy diffusivity; $R$ is the vertical profile of the penetrating shortwave radiation

[*Paulson and Simpson*, 1977]; and $C_p$ is the specific heat of water at constant pressure. Note that the vertical derivative in the physical coordinates $\partial/\partial z = (1/H_z)\partial/\partial s$. We show these details here to emphasize that diagnostic analyses using standard ROMS outputs must be done with care, in particular, when tides are resolved and $H_z$ changes appreciably over the averaging interval. The standard ROMS outputs time-average terms in (1) normalized by $H_z$ averaged over the same interval. More specifically, if we denote the averaging over the 2-hr interval as $\langle ... \rangle$, then ROMS outputs:

(a) the tendency term, $(1/\langle H_z \rangle)\langle$lhs of (1)$\rangle$;

(b) the sum of "horizontal and vertical advective terms", $\langle \{...\} \rangle / \langle H_z \rangle$, where $\{...\}$ denote the first group of terms on the rhs of (1). Note that this term is a divergence of the advective fluxes through the sides of each computational cell rather than advection. Also note horizontal and vertical advection terms are combined in our analysis, in particular, since it is hard to interpret "vertical advection" (more exactly, the vertical divergence in the temperature flux) through the moving s-surfaces separately.

(c) the "vertical diffusion" term, $\langle [...] \rangle / \langle H_z \rangle$, where [...] denote the second group of terms on the rhs of (1). Note that in the standard ROMS output, the vertical diffusion is combined with the vertical divergence in the penetrating shortwave radiation.

These diagnostic terms are analyzed in a meridional section at 175˚ W, immediately east of Atka Pass. The main goal is to demonstrate that both advective and vertical mixing terms can contribute to warming on the 26.8 kg $m^{-3}$ isopycnal surface over the slope. The time-integrated tendency term is approximately the difference between temperature fields at the beginning and

end of a specified interval. To avoid incorrect inferences due to the tide-induced changes on the slope, we first low pass filter the time series of each diagnostic term at each point using a 40-hr half-amplitude filter. The resulting time series, with tides removed, are integrated over a two-month period including July and August. The subsequent time-integrated terms, in units of ˚C, are shown in Figure 7 and in a close-up on the north slope in Figure 8. Analysis and discussion of the temperature diagnostic terms in the upper 50 m will be left for the future. Here we will focus on the core of the ANSC and the slope in the vicinity of $\sigma_\theta$ =26.8 kg m$^{-3}$.

Within the ANSC area, inshore of 52.4˚N (see Figure 8a), the temperature change is positive over this time period. Below the surface boundary layer, this warming trend is supported by the advective term (Figure 8b). Inshore of 52.3˚N, close to the slope, the vertical diffusion term (Figure 8c) works to redistribute the heat by cooling the jet core and warming the waters in the lower part of the jet, between 150 and 300 m. The 26.8 kg m$^{-3}$ isopycnal surface (shown as the 2-month mean plus-minus one standard deviation) is found between 150-300 m over the slope half of the time. When uplifted, it receives the heat from the advective core above, which is then advected farther east or offshore with the separating eddies.

Over the deep basin to the north of the slope (Figure 7a), the change in temperature between 50-400 m can be fully accounted for by advection (Figure 7b), and associated with the slowly evolving mesoscale eddies. Away from the slope and below 80 m depth, the time integrated vertical diffusion term (Figure 7c) is nearly zero. On $\sigma_\theta$ =26.8 kg m$^{-3}$ advection is weaker than it is closer to the surface, but non-negligible (contributing to 0.2 ˚C changes over a span of 2 months).

*2.3.4 Locations of intensified warmer water separation from ANSC to the deep basin*

To evaluate the continuity of the temperature structure on $\sigma_{26.8}$ and determine times and locations of flow separation, we examine the along-slope variability in the meridionally-averaged $T_{26.8}$. The meridional average is taken from the axis of the island arc to positions 65 km to the north, across the black box contoured in Figure 4 (top). The resulting cross-shore-averaged $T_{26.8}$ is plotted as a function of the longitude and time (Figure 9). The sloping streaks of similar temperature observed in Figure 9, particularly east of 178˚W (Amukta Pass), indicate advection of the temperature anomaly. The warmer temperature patterns that persist at approximately fixed longitudes in Figure 9 are indicative of "centers" where warm water extends father offshore. These are located at 178˚W, 174˚W, and next to Amukta Pass (170-172˚ W).

The anomaly at 178˚W is an indicator of warm water separating from the ANSC into the Bering Sea basin as a topographic effect on the northern slope just upstream of this location (Figure 10, top). The abrupt change in bathymetry forces the flow to spin off of the slope into the basin in an eddy-like structure, filling the 65-km averaging band with the warmer water. A similar effect is seen at 174˚W (Figure 10, bottom) where the northern coast of Atka Island protrudes far north.

The third area where $T_{26.8}$ over the slope is found to be relatively warmer than upstream is a region immediately north of Amukta Pass, 170-172˚ W (see Figure 9). Temperature variability here is different from the two separation centers discussed above and is strongly influenced by the tides. In particular, the high-frequency oscillations associated with the diurnal tide are especially visible, as well as the approximately 14-day modulation due to the spring and neap diurnal tides. This modulation results from the interaction of two processes: enhanced vertical mixing during peak tide that transports heat to $\sigma_\theta$ =26.8 kg m$^{-3}$ and subsequent

northward near-bottom tidal current that flushes the warmer water into the Bering Sea Basin. These processes are most vigorous and combine most effectively during the periods of spring tide, when $K_1$ and $O_1$ variations in the sea level are in phase over the pass. These assertions are illustrated with Figure 11 that shows cross-pass (i.e. west-east) instantaneous sections of the temperature, along-pass (i.e. northward) velocity, and the logarithm of vertical eddy diffusivity. Panels on the left correspond to the time of peak northward transport over the tidal cycle and plots on the right are for the time instance 8 hours later. The cycle selected is representative of peak spring tide conditions. Note that water denser than $\sigma_\theta$ =26.8 kg m$^{-3}$ is found in this section only intermittently and only in the deepest part of the pass, close to the eastern flank. During the time of the peak northward flow, the vertical diffusivity coefficient in the eastern portion of the channel is large throughout most of the water column, indicating enhanced vertical mixing (Fig. 11c). However, the core of the northward jet is just above the $\sigma_\theta$ =26.8 kg m$^{-3}$ contour (Fig. 11b). Eight hours later, the integrated transport through the pass is much weaker, but the northward jet is formed near bottom (Fig. 11e), flushing some of the densest waters found in the pass into the Bering Sea. During the neap tide period (not shown), the tidal mixing is much weaker. Also note that mixing event over the tidal cycle is very intermittent. For instance, *Durski et al.* [2015] show patterns of density in the same section, detided and averaged over several spring and neap tide periods. It turns out that during the periods of spring tides the average stratification in the pass is stronger due to the stronger inflow of warmer and fresher waters from the Pacific.

### *2.3.5 Backward Particle Tracking*

A motivation for this study was the hypothesis (due to Stabeno et al. [2009]) that the source of the warm water in the temperature maximum layer observed in the south-east corner of the Bering Sea basin is found in Amukta Pass. To corroborate this, we perform a backward particle tracking experiment on $\sigma_\theta = 26.8$ kg m$^{-3}$. Specifically, within the Bering Canyon area shown as the black box in Figure 12, 200 starting particle positions were randomly selected on each of the following dates – October 15, October 20, October 25, and October 30 (for a total of 800 particles) – and tracked backwards in time for 106 days. Results from this experiment are consistent with those from the previously discussed forward particle tracking experiments. Very few particles (2%) passed through Amukta Pass from the Alaskan Stream on their way to the Bering Canyon. Approximately 8% of particles registered their location in Amukta Pass, even though only 2% of particles actually pass through it. Many of the particles that eventually reach the Bering Canyon region were backtracked at locations west of Amukta Pass.

This experiment shows evidence of the westward countercurrent along the line from Pribilof Canyon toward Atka Pass first reported by *Ladd* [2014] based on altimetry analysis. In these backtracking experiments, many particles fail to leave the release area due to long residence times of eddies within the Bering Canyon. Particle tracking also shows vigorous eddy activity near Pribilof Canyon, where warmer BSC waters can also separate into the basin supporting the subsurface temperature maximum. Once again, current speeds on this surface are not fast enough to backtrack the particles from the Bering Canyon to the Alaskan Stream past Amchitka Pass.

The pdf for this backward Lagrangian particle experiment (Figure 13), calculated with the same procedure as for the forward particle tracking experiments, reveals that the majority of particles either followed the path of the ANSC or resided for long periods within the Bering

Canyon region. Of the particles with paths extending west of Amukta Pass, many came from the Amchitka Pass area in the ANSC, although none passed through Amchitka Pass within the 106-day periods of the particle tracking experiments. The path of the westward countercurrent bounds the area of non-zero pdf from the north between 169-175˚ W.

**2.4 Summary.**

A high-resolution circulation model for the Eastern Bering Sea was used to understand mechanisms and patterns of slope - interior ocean exchange along the path of the ANSC that may bring heat to the level of the subsurface temperature maximum on the isopycnal surface $\sigma_\theta$ =26.8 kg m$^{-3}$. The hypothesis, due to [*Stabeno et al.*, 2009], that the subsurface maximum waters can originate in Amukta Pass, is confirmed by the analysis of temperature patterns on this isopycnal surface and forward and backward Lagrangian particle tracking analyses. However, the model analysis suggests that direct advection of warmer Pacific waters over the pass at this density level is very limited. It is more likely that the water masses entrained at $\sigma_\theta = 26.8$ kg m$^{-3}$ from the area of Amukta Pass into the ANSC are formed as a result of intensive tidal mixing in the pass. Warm water intrusions into the ANSC at that level from the pass are strongly modulated at the temporal scales of the diurnal tides and the $K_1$-$O_1$ spring-neap cycle.

Amukta Pass is not the only location along the rim of the Bering Sea basin where flow can separate into the basin interior at that level. Our model analyses demonstrate substantial intrusions through the deep and wide Amchitka Pass at 180˚W where warmer Pacific subsurface waters get entrained in large eddies along Bowers Ridge and recirculations around islands north

of the pass. Along the path of ANSC, two separation points are found, at 178˚W and 174˚W where the current is deflected away from the slope by topographic features.

Particle tracking experiments indicate that warming of the ANSC on $\sigma_\theta = 26.8$ kg m$^{-3}$ cannot be explained as along-isopycnal transport from warmer regions. Transport on the shallower $\sigma_\theta = 26.4$ kg m$^{-3}$ isopycnal surface is fast enough to bring warm water along the southern Aleutian island slope, through Amchitka Pass and into the ANSC between June and October. These shallower waters can also cross into the Bering Sea through the passes east of Amchitka. In the shallow passes, the heat from above is intermittently mixed downward and then flushed into the ANSC core, at 50-200 m below the surface. Tide-induced vertical mixing over the slope helps to transport heat to the deeper layers, including $\sigma_\theta = 26.8$ kg m$^{-3}$. This is confirmed by the heat equation term balance analysis. It indicates that increase in the temperature at the level of the 26.8 kg m$^{-3}$ isopycnal on the north slope results from the combined effects of advection and vertical diffusion. The vertical diffusion term is positive in the shallower range of the mean ± one standard deviation depth of the isopycnal. Since the 26.8 kg m$^{-3}$ isopycnal is below the influence of surface cooling and heating [*Johnson et al.*, 2004], these mechanisms are especially important in the summer months. In winter, the reverse process might be anticipated if surface temperatures were cold enough. But even in winter surface water temperatures don't tend to fall below the range of the subsurface maximum based on monthly average SST from OSTIA satellite estimates for winter 2009-10 [*Donlon et al.*, 2012].

This model run has proved useful in evaluating the role of slope-interior exchange in the maintenance of the observed subsurface temperature maximum layer in the Bering Sea. This study encourages a similar evaluation with a full year model run. In particular, results of the

Lagrangian particle analyses can be extended to help explaining transport of larvae of halibut and other species along the Bering Sea slope [*Sohn et al.*, 2010; *Vestfals et al.*, 2014].

The baroclinic Rossby radius of deformation in the Bering Sea is estimated to be as small as 20 km [*Chelton et al.*, 1998; *Stabeno et al.*, 2005]. Our model resolves this scale, but may be too coarse to represent submesoscale instabilities and filamentation on the slope [*Molemaker et al.*, 2014] and in the oceanic basin [*Capet et al.*, 2008]. Simulations at a higher, sub-kilometer resolution will show if submesoscale variability alters slope-interior ocean exchange along ANSC and BSC.

**2.5 References.**

Argo (2000), Argo float data and metadata from Global Data Assembly Centre (Argo GDAC), , doi:10.17882/42182.

Capet, X., J. C. McWilliams, M. J. Molemaker, and A. F. Shchepetkin (2008), Mesoscale to Submesoscale Transition in the California Current System. Part I: Flow Structure, Eddy Flux, and Observational Tests, *J. Phys. Oceanogr.*, *38*(1), 29–43, doi:10.1175/2007JPO3671.1.

Chapman, D. C. (1985), Numerical Treatment of Cross-Shelf Open Boundaries in a Barotropic Coastal Ocean Model, *J. Phys. Oceanogr.*, *15*(8), 1060–1075, doi:10.1175/1520-0485(1985)015<1060:NTOCSO>2.0.CO;2.

Chassignet, E. P., H. E. Hurlburt, O. M. Smedstad, G. R. Halliwell, P. J. Hogan, A. J. Wallcraft, R. Baraille, and R. Bleck (2007), The HYCOM (HYbrid Coordinate Ocean Model) data assimilative system, *Journal of Marine Systems*, *65*(1–4), 60–83, doi:10.1016/j.jmarsys.2005.09.016.

Chelton, D. B., R. A. deSzoeke, M. G. Schlax, K. El Naggar, and N. Siwertz (1998), Geographical Variability of the First Baroclinic Rossby Radius of Deformation, *J. Phys. Oceanogr.*, *28*(3), 433–460, doi:10.1175/1520-0485(1998)028<0433:GVOTFB>2.0.CO;2.

Clement, J. L., W. Maslowski, L. W. Cooper, J. M. Grebmeier, and W. Walczowski (2005), Ocean circulation and exchanges through the northern Bering Sea—1979–2001 model results, *Deep Sea Research Part II: Topical Studies in Oceanography*, *52*(24), 3509–3540, doi:10.1016/j.dsr2.2005.09.010.

Clement Kinney, J., and W. Maslowski (2012), On the oceanic communication between the Western Subarctic Gyre and the deep Bering Sea, *Deep Sea Research Part I: Oceanographic Research Papers*, *66*, 11–25, doi:10.1016/j.dsr.2012.04.001.

Clement Kinney, J., W. Maslowski, and S. Okkonen (2009), On the processes controlling shelf–basin exchange and outer shelf dynamics in the Bering Sea, *Deep Sea Research Part II: Topical Studies in Oceanography*, *56*(17), 1351–1362, doi:10.1016/j.dsr2.2008.10.023.

Danielson, S., E. Curchitser, K. Hedstrom, T. Weingartner, and P. Stabeno (2011), On ocean and sea ice modes of variability in the Bering Sea, *J. Geophys. Res.*, *116*(C12), C12034, doi:10.1029/2011JC007389.

Danielson, S., T. Weingartner, K. Aagaard, J. Zhang, and R. Woodgate (2012), Circulation on the central Bering Sea shelf, July 2008 to July 2010, *J. Geophys. Res.*, *117*(C10), C10003, doi:10.1029/2012JC008303.

Danielson, S. L., T. J. Weingartner, K. S. Hedstrom, K. Aagaard, R. Woodgate, E. Curchitser, and P. J. Stabeno (2014), Coupled wind-forced controls of the Bering–Chukchi shelf circulation and the Bering Strait throughflow: Ekman transport, continental shelf waves, and variations of the Pacific–Arctic sea surface height gradient, *Progress in Oceanography*, *125*, 40–61, doi:10.1016/j.pocean.2014.04.006.

Donlon, C. J., M. Martin, J. Stark, J. Roberts-Jones, E. Fiedler, and W. Wimmer (2012), The Operational Sea Surface Temperature and Sea Ice Analysis (OSTIA) system, *Remote Sensing of Environment*, *116*, 140–158, doi:10.1016/j.rse.2010.10.017.

Durski, S., A. Kurapov, J. Zhang, and G. Panteleev (2015), Circulation in the Eastern Bering Sea: Inferences from a 2-km-resolution model, *ResearchGate*, doi:http://dx.doi.org/10.1016/j.dsr2.2015.02.002.

Egbert, G. D., and S. Y. Erofeeva (2002), Efficient Inverse Modeling of Barotropic Ocean Tides, *J. Atmos. Oceanic Technol.*, *19*(2), 183–204, doi:10.1175/1520-0426(2002)019<0183:EIMOBO>2.0.CO;2.

Ezer, T., and L.-Y. Oey (2010), The Role of the Alaskan Stream in Modulating the Bering Sea Climate, *Journal of Geophysical Research: Oceans*, doi:10.1029/2009jc005830.

Fairall, C. W., E. F. Bradley, J. E. Hare, A. A. Grachev, and J. B. Edson (2003), Bulk Parameterization of Air–Sea Fluxes: Updates and Verification for the COARE Algorithm, *J. Climate*, *16*(4), 571–591, doi:10.1175/1520-0442(2003)016<0571:BPOASF>2.0.CO;2.

Favorite, F. (1974), Flow into the Bering Sea through Aleutian island passes, in *Oceanography of the Bering Sea With Emphasis on Renewable Resources*, edited by D. W. Hood and E. J. Kelley, pp. 3–37, Institute of Marine Science, University of Alaska, Fairbanks, Alaska.

Flather, R. A. (1976), *A tidal model of the north-west European continental shelf*.

Foreman, M. G. G., P. F. Cummins, J. Y. Cherniawsky, and P. Stabeno (2006), Tidal energy in the Bering Sea, *Journal of Marine Research*, *64*(6), 797–818, doi:10.1357/002224006779698341.

Hu, H., and J. Wang (2010), Modeling effects of tidal and wave mixing on circulation and thermohaline structures in the Bering Sea: Process studies, *J. Geophys. Res.*, *115*(C1), C01006, doi:10.1029/2008JC005175.

Hunt, G. L., P. J. Stabeno, S. Strom, and J. M. Napp (2008), Patterns of spatial and temporal variation in the marine ecosystem of the southeastern Bering Sea, with special reference to the Pribilof Domain, *Deep Sea Research Part II: Topical Studies in Oceanography*, *55*(16), 1919–1944, doi:10.1016/j.dsr2.2008.04.032.

Johnson, G. C., P. J. Stabeno, and S. C. Riser (2004), The Bering Slope Current System Revisited*, *J. Phys. Oceanogr.*, *34*(2), 384–398, doi:10.1175/1520-0485(2004)034<0384:TBSCSR>2.0.CO;2.

Kantha, L. H., and C. A. Clayson (1994), An improved mixed layer model for geophysical applications, *J. Geophys. Res.*, *99*(C12), 25235–25266, doi:10.1029/94JC02257.

Kowalik, Z. (1999), Bering Sea tides, in *Dynamics of the Bering Sea*, edited by T. R. Loughlin and K. Ohtani, pp. 93–127, University of Alaska Sea Grant, Fairbanks, Alaska.

Ladd, C. (2014), Seasonal and interannual variability of the Bering Slope Current, *Deep Sea Research Part II: Topical Studies in Oceanography*, *109*, 5–13, doi:10.1016/j.dsr2.2013.12.005.

Li, L., A. J. Miller, J. L. McClean, I. Eisenman, and M. C. Hendershott (2014), Processes driving sea ice variability in the Bering Sea in an eddying ocean/sea ice model: anomalies from the mean seasonal cycle, *Ocean Dynamics*, *64*(12), 1693–1717, doi:10.1007/s10236-014-0769-7.

Mellor, G. L., and T. Yamada (1982), Development of a turbulence closure model for geophysical fluid problems, *Rev. Geophys.*, *20*(4), 851–875, doi:10.1029/RG020i004p00851.

Mesinger, F. et al. (2006), North American Regional Reanalysis, *Bull. Amer. Meteor. Soc.*, *87*(3), 343–360, doi:10.1175/BAMS-87-3-343.

Molemaker, M. J., J. C. McWilliams, and W. K. Dewar (2014), Submesoscale Instability and Generation of Mesoscale Anticyclones near a Separation of the California Undercurrent, *J. Phys. Oceanogr.*, *45*(3), 613–629, doi:10.1175/JPO-D-13-0225.1.

Nakamura, T., Y. Isoda, H. Mitsudera, S. Takagi, and M. Nagasawa (2010), Breaking of unsteady lee waves generated by diurnal tides, *Geophys. Res. Lett.*, *37*(4), L04602, doi:10.1029/2009GL041456.

Panteleev, G., M. Yaremchuk, V. Luchin, D. Nechaev, and T. Kukuchi (2012), Variability of the Bering Sea circulation in the period 1992–2010, *J Oceanogr*, *68*(4), 485–496, doi:10.1007/s10872-012-0113-0.

Paulson, C. A., and J. J. Simpson (1977), Irradiance Measurements in the Upper Ocean, *J. Phys. Oceanogr.*, *7*(6), 952–956, doi:10.1175/1520-0485(1977)007<0952:IMITUO>2.0.CO;2.

Reed, R. K., and P. J. Stabeno (1999), The Aleutian North Slope Current, in *Dynamics of the Bering Sea*, edited by T. R. Loughlin and K. Ohtani, pp. 177–191, University of Alaska Sea Grant, Fairbanks, Alaska.

Roden, G. I. (1995), Aleutian Basin of the Bering Sea: Thermohaline, oxygen, nutrient, and current structure in July 1993, *J. Geophys. Res.*, *100*(C7), 13539–13554, doi:10.1029/95JC01291.

Schmoldt, A., H. F. Benthe, and G. Haberland (1975), Digitoxin metabolism by rat liver microsomes, *Biochem. Pharmacol.*, *24*(17), 1639–1641.

Shchepetkin, A. F., and J. C. McWilliams (2003), A method for computing horizontal pressure-gradient force in an oceanic model with a nonaligned vertical coordinate, *J. Geophys. Res.*, *108*(C3), 3090, doi:10.1029/2001JC001047.

Shchepetkin, A. F., and J. C. McWilliams (2005), The regional oceanic modeling system (ROMS): a split-explicit, free-surface, topography-following-coordinate oceanic model, *Ocean Modelling*, *9*(4), 347–404, doi:10.1016/j.ocemod.2004.08.002.

Sohn, D., L. Ciannelli, and J. T. Duffy-Anderson (2010), Distribution and drift pathways of Greenland halibut (Reinhardtius hippoglossoides) during early life stages in the eastern Bering Sea and Aleutian Islands: Distribution and drift pathways of Greenland halibut, *Fisheries Oceanography*, *19*(5), 339–353, doi:10.1111/j.1365-2419.2010.00549.x.

Stabeno, P. J., D. J. Schumacher, and K. Ohtani (1999), The Physical oceanography of the Bering Sea, in *Dynamics of the Bering Sea*, edited by T. R. Loughlin and K. Ohtani, pp. 1–28, University of Alaska Sea Grant, Fairbanks, Alaska.

Stabeno, P. J., D. G. Kachel, N. B. Kachel, and M. E. Sullivan (2005), Observations from moorings in the Aleutian Passes: temperature, salinity and transport, *Fisheries Oceanography*, *14*, 39–54, doi:10.1111/j.1365-2419.2005.00362.x.

Stabeno, P. J., C. Ladd, and R. K. Reed (2009), Observations of the Aleutian North Slope Current, Bering Sea, 1996–2001, *J. Geophys. Res.*, *114*(C5), C05015, doi:10.1029/2007JC004705.

Vestfals, C. D., L. Ciannelli, J. T. Duffy-Anderson, and C. Ladd (2014), Effects of seasonal and interannual variability in along-shelf and cross-shelf transport on groundfish recruitment in the eastern Bering Sea, *Deep Sea Research Part II: Topical Studies in Oceanography*, *109*, 190–203, doi:10.1016/j.dsr2.2013.09.026.

Walsh, J. E., W. L. Chapman, and D. H. Portis (2009), Arctic Cloud Fraction and Radiative Fluxes in Atmospheric Reanalyses, *J. Climate*, *22*(9), 2316–2334, doi:10.1175/2008JCLI2213.1.

Zhang, J., R. Woodgate, and R. Moritz (2010), Sea Ice Response to Atmospheric and Oceanic Forcing in the Bering Sea, *J. Phys. Oceanogr.*, *40*(8), 1729–1747, doi:10.1175/2010JPO4323.1.

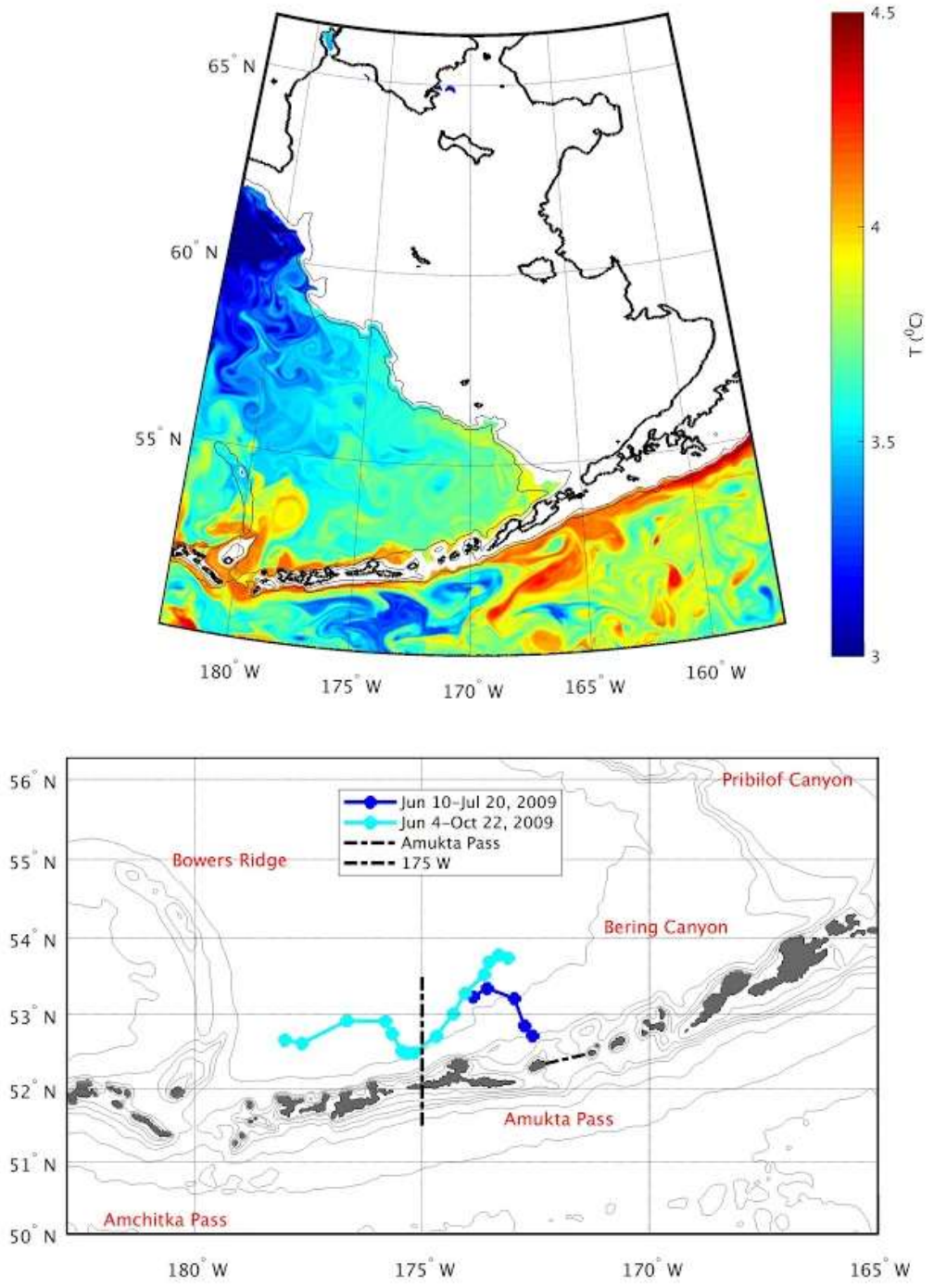


*Figure 1 (Top) The model domain with daily averaged temperature on $\sigma_\theta$ =26.8 kg m$^{-3}$ shown for September 29, 2009 with 200, 1000 m isobaths contoured (black). (Bottom) Subsection of model domain with 100, 200, 500, 1000, 3000, and 5000 m isobaths contoured (gray), selected Argo float tracks (blue, cyan), and model transect locations (black).*

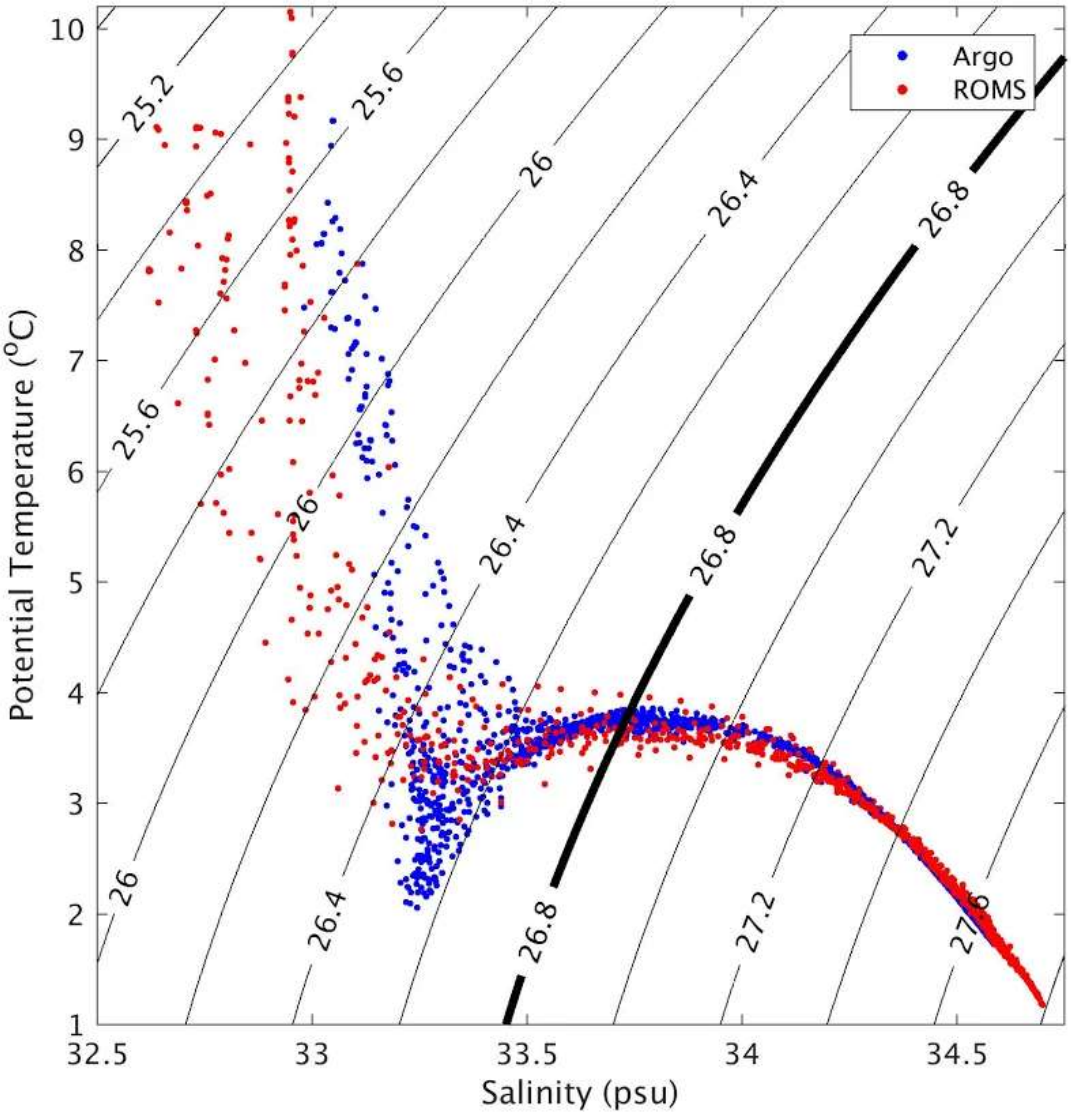


*Figure 2 Temperature-Salinity plot from 20 profiles of two ARGO floats, Jun 4- Oct 22, 2009 (blue), and corresponding model profiles, sampled at ARGO locations and times (red). Black contours are the potential density (kg $m^{-3}$).*

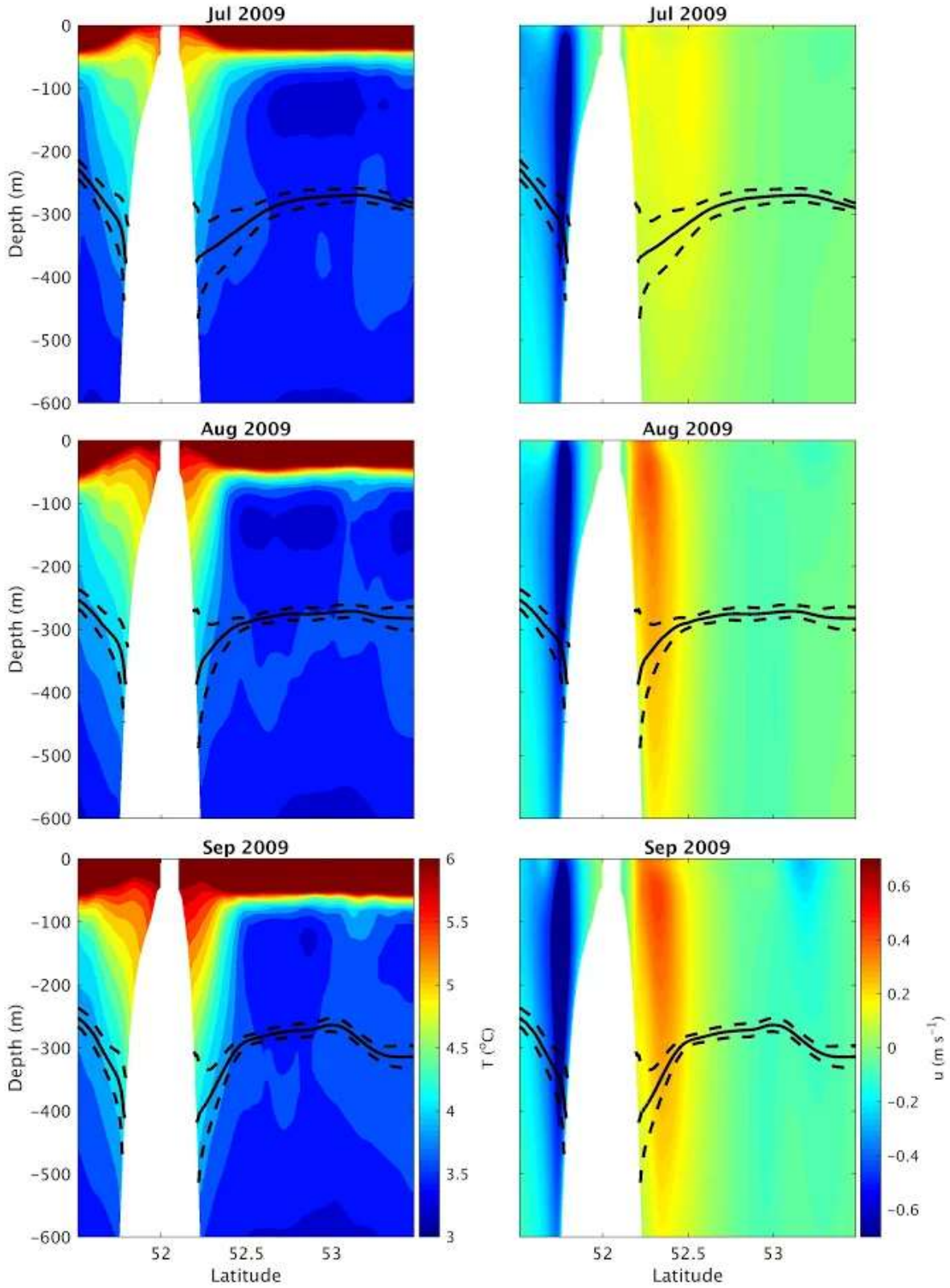


*Figure 3 Meridional sections of (left) the monthly averaged temperature and (right) the zonal current component across the Aleutian Arc at 175˚W. The 26.8 kg $m^{-3}$ isopycnal location is shown as the monthly mean (bold line) ± 1 standard deviation (dashed line).*

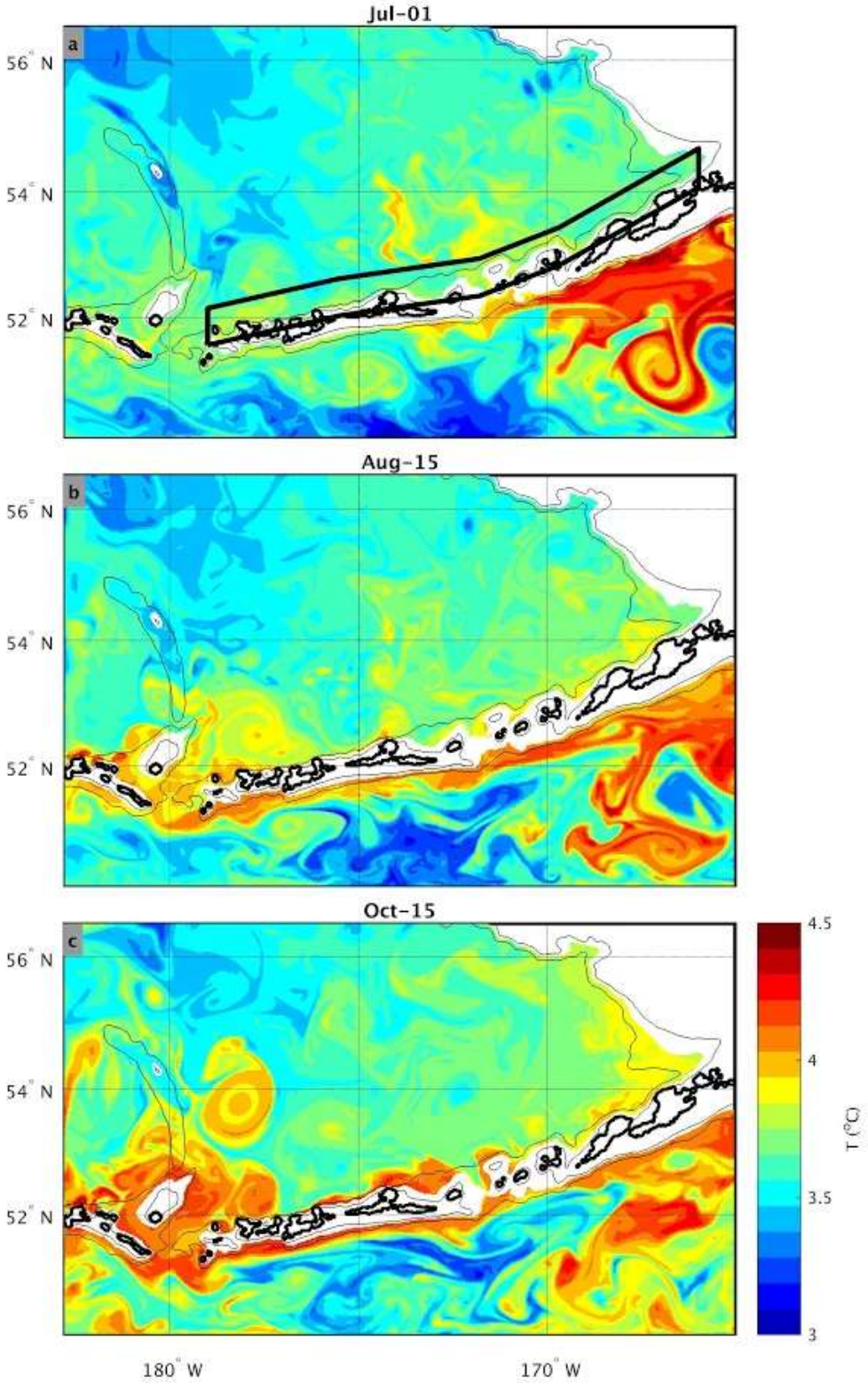


*Figure 4 Daily averaged temperature on the 26.8 kg $m^{-3}$isopycnal surface with 200 m and 1000 m isobaths contoured (thin black). The black box in panel (a) is the analysis area with reference to Figure 9.*

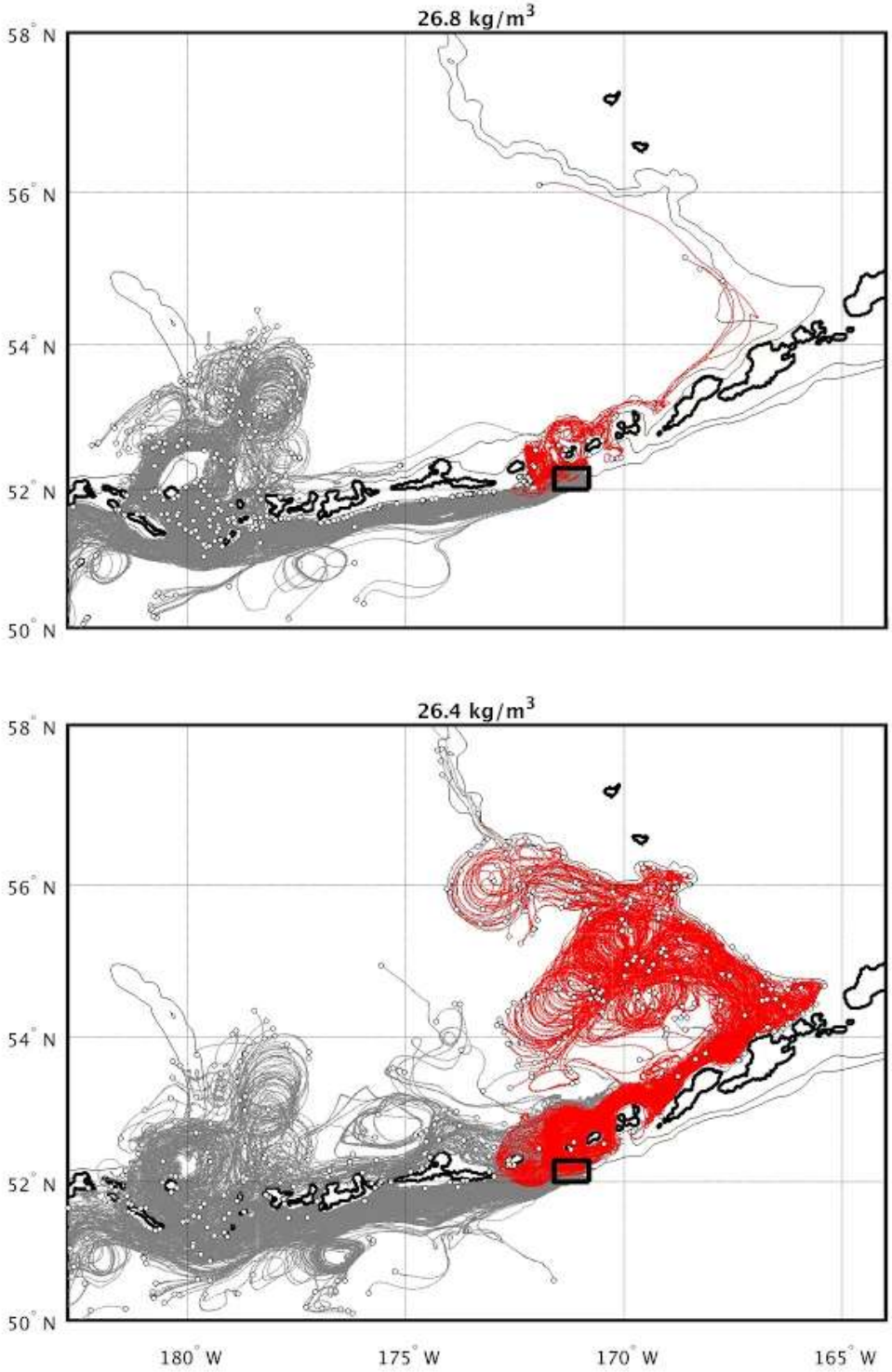


*Figure 5 Trajectories of the Lagrangian particles released near Amukta Pass (black box) on the 26.8 kg $m^{-3}$ (top) and 26.4 kg $m^{-3}$ (bottom) isopycnals and tracked forward on the respective isopycnal surfaces for 92 days. End locations are shown as white circles. Red paths indicate particles that have traveled through Amukta Pass.*

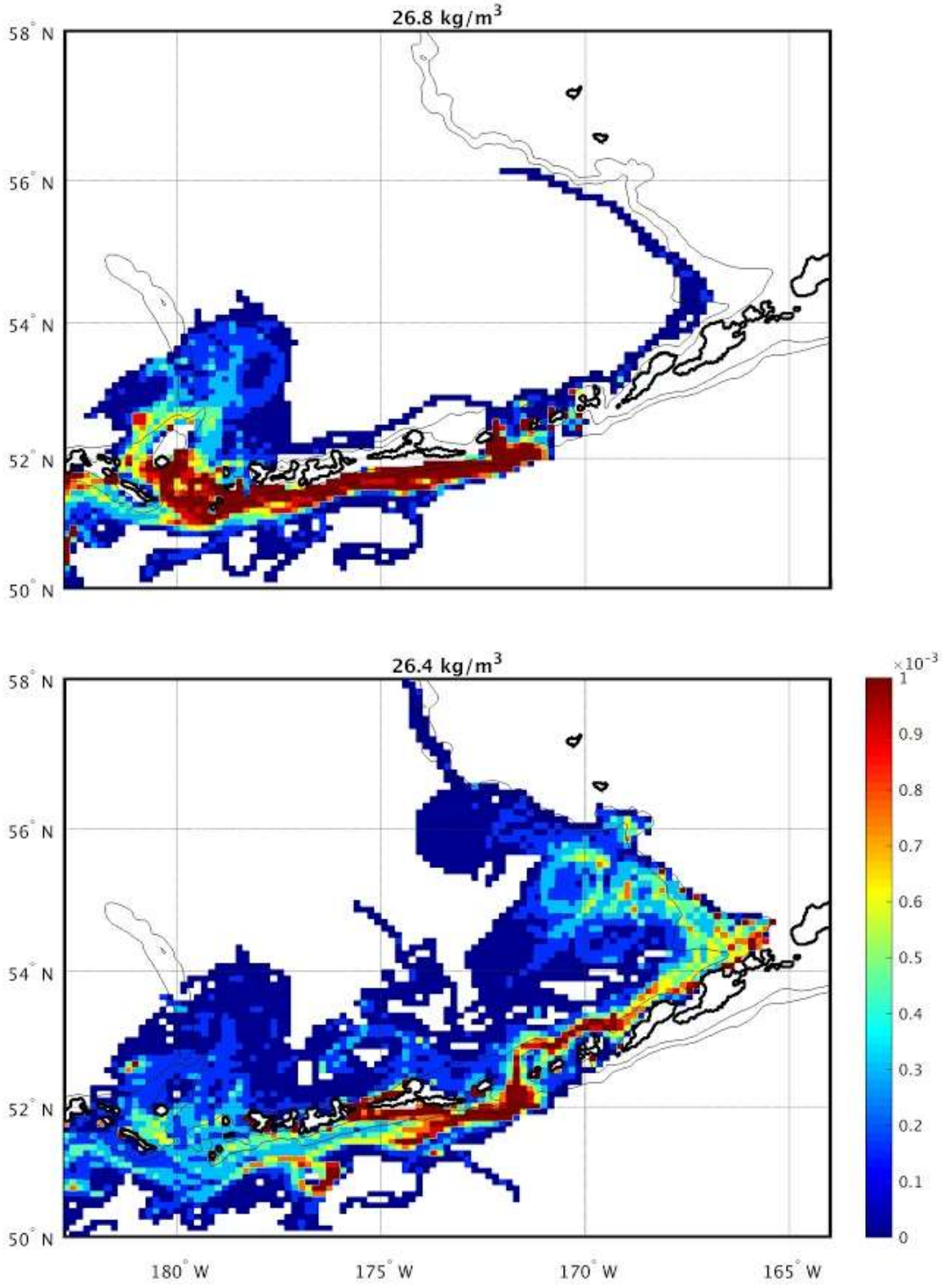


*Figure 6 PDFs of particle positions on the 26.8 kg $m^{-3}$ (top) and 26.4 kg $m^{-3}$ (bottom) isopycnal, based on the forward Lagrangian tracking experiments.*

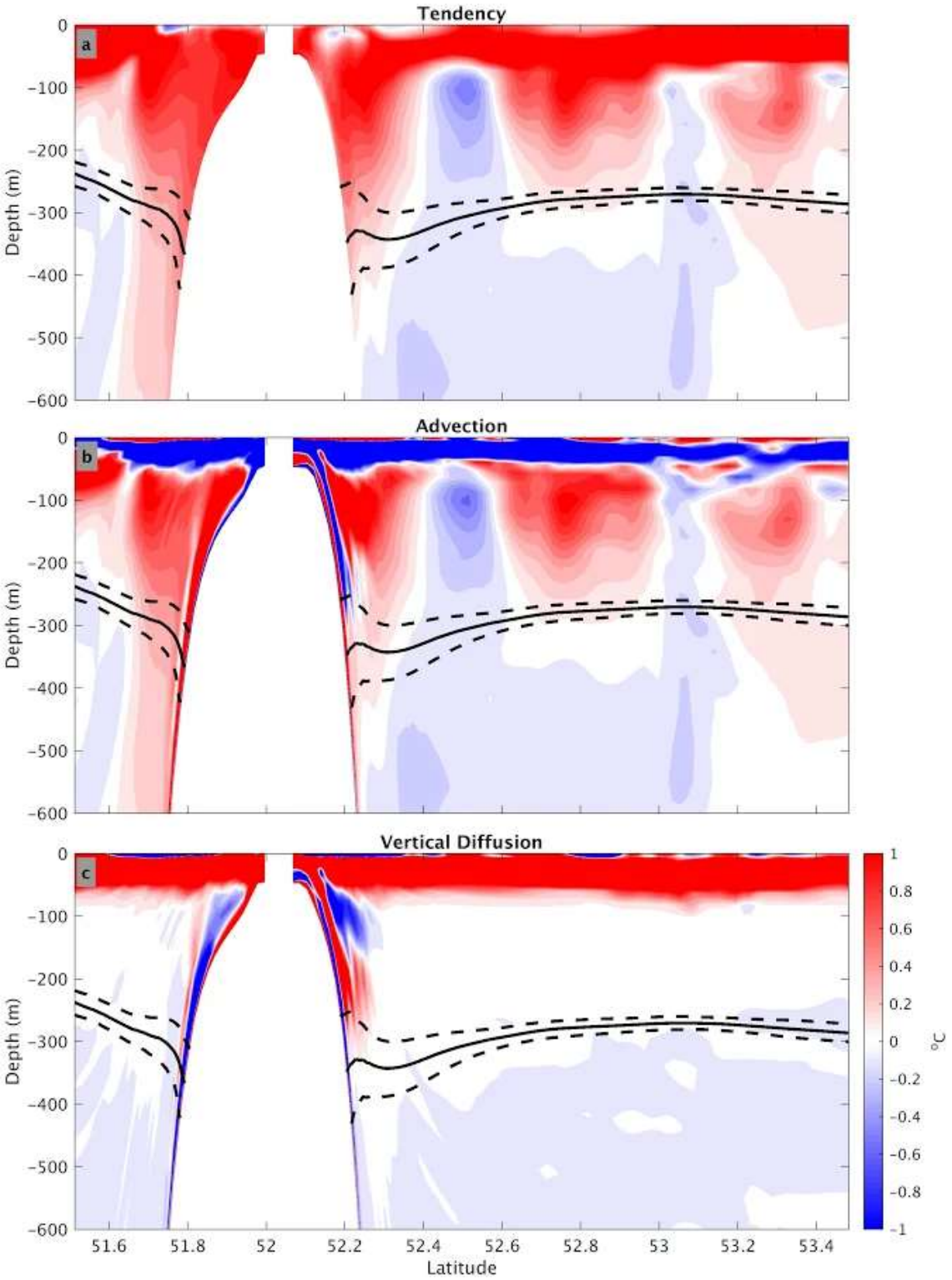


*Figure 7 Time-integrated terms in the heat equation, July-August 2009: (Top) Tendency, (Middle) advective term, (Bottom) vertical diffusion term combined with the penetrating shortwave radiation term. Note the time series for each term were low-pass filtered to remove the tides before the time integration. The 26.8 kg $m^{-3}$isopycnal surface location is shown as the two-month mean (bold line) ± 1 standard deviation (dashed line).*

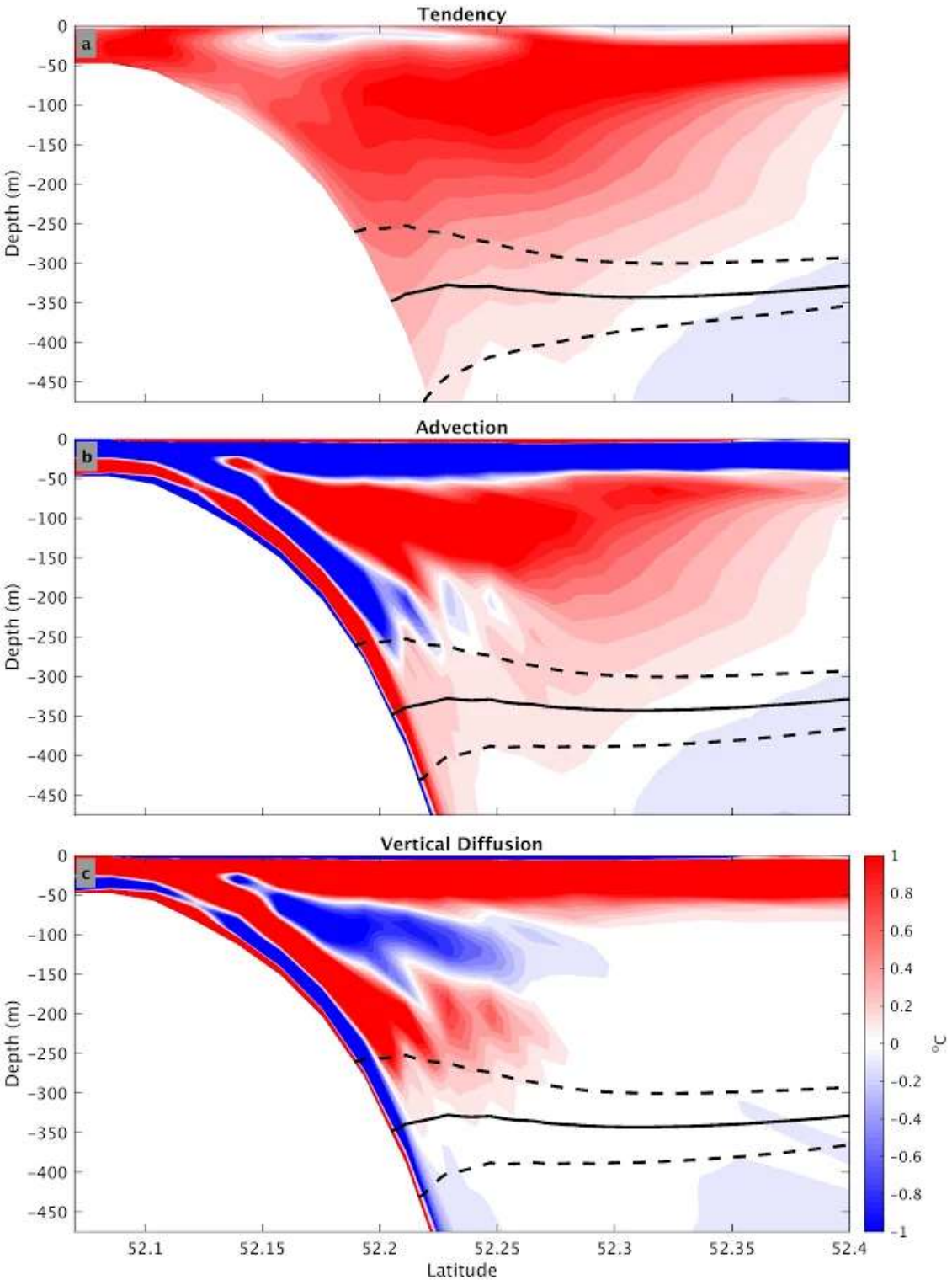


*Figure 8. Same as Figure 7, zoomed on the ANSC area.*

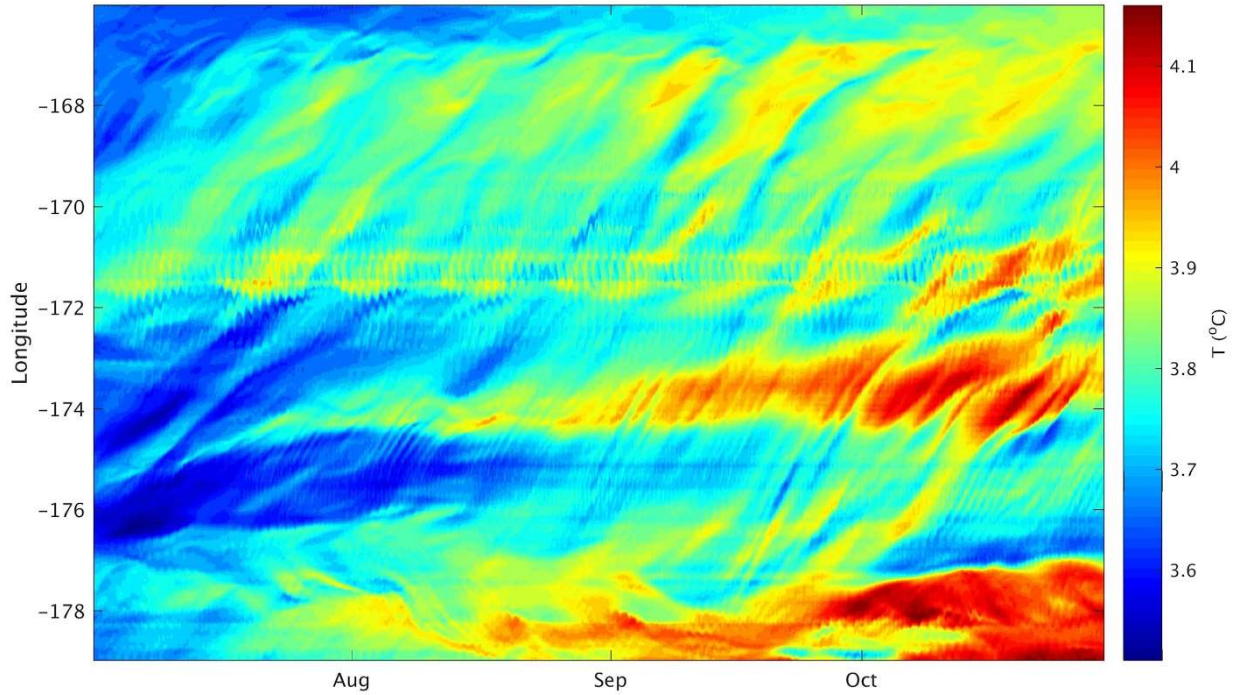


*Figure 9 Meridionally averaged (within the area shown in Figure 4) temperature on the 26.8 kg $m^{-3}$isopycnal over the path of ANSC shown as a function of time and longitude. Temporal resolution is 2 hours.*

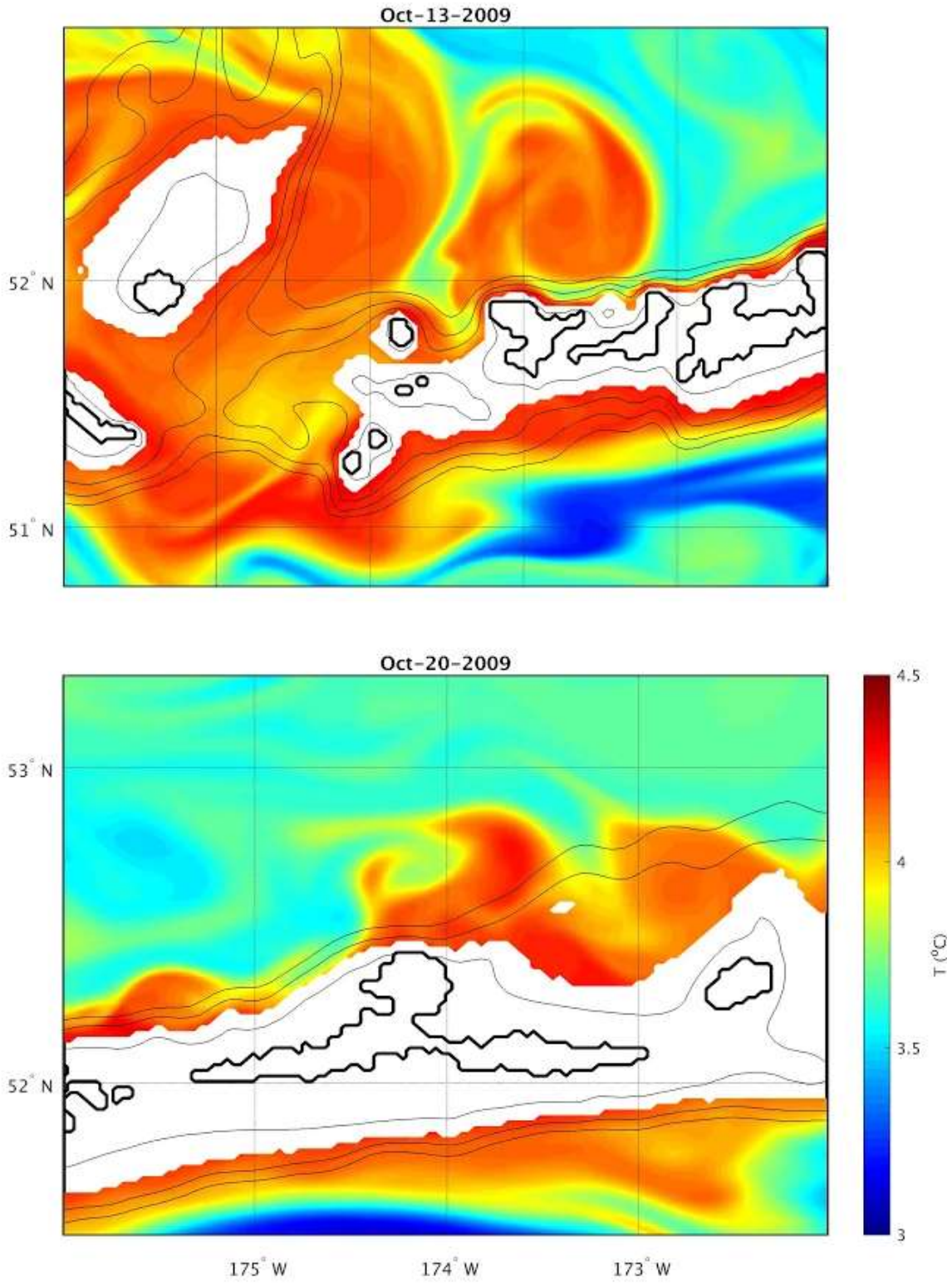


*Figure 10 (Top) Daily averaged temperature patterns on $\sigma_\theta$ =26.8 kg m$^{-3}$ showing flow separation near: (top) 178° W, (bottom) 174° W. Thin black contours are 200 m, 1000 m, 1500m, and 2000 m isobaths.*

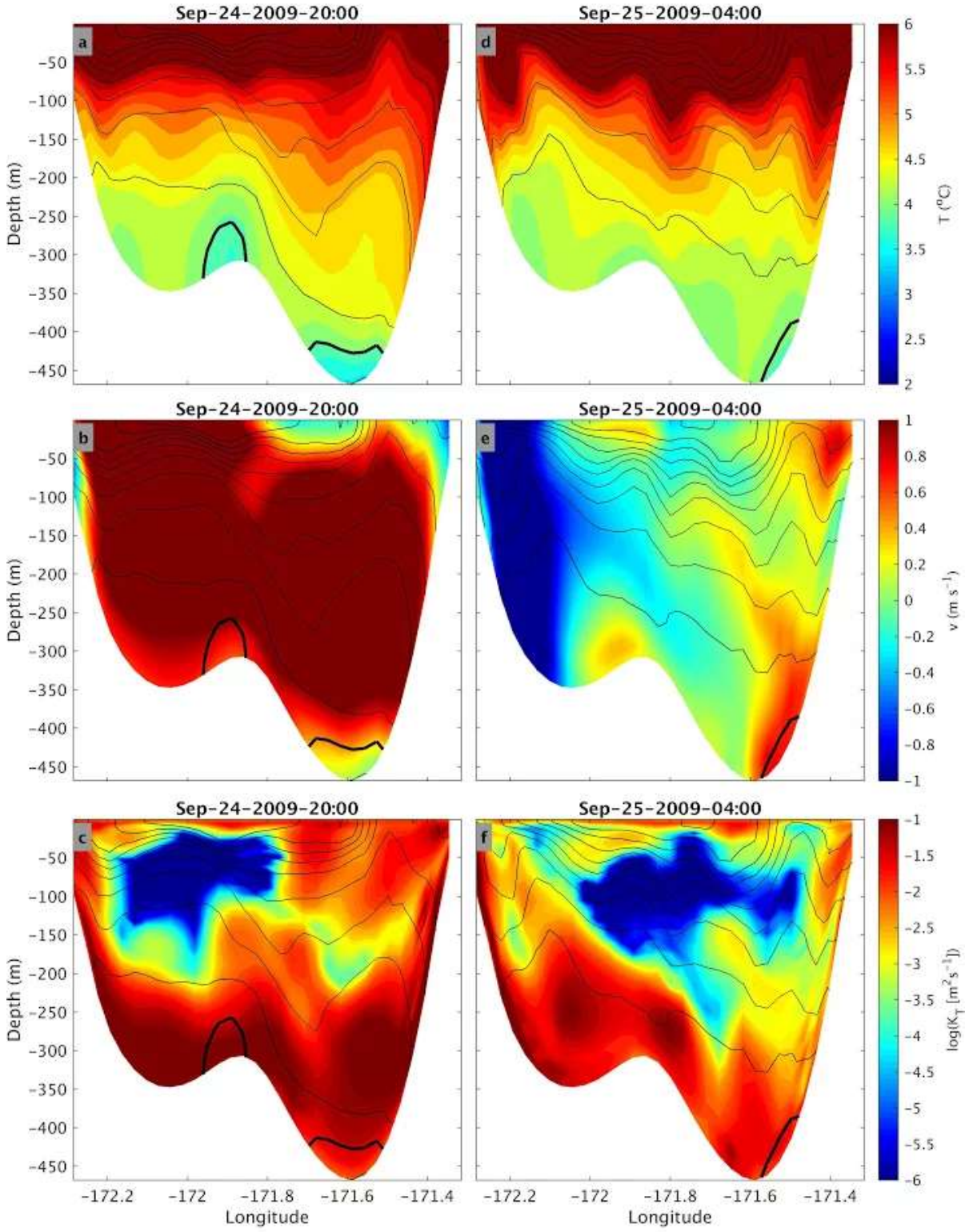


*Figure 11 Instantaneous oceanic fields in the zonal section across Amukta pass: (top) temperature, (middle) northward velocity, and (bottom) $\log_{10}$ of the vertical diffusivity coefficient. (LEFT) September 24 2009, 20:00 UTC, corresponding to the largest transport through the pass, and (RIGHT) September 25 2009, 04:00 UTC, corresponding to the highest tidal elevation in the pass. Density (black lines) is contoured every 0.2 kg $m^{-3}$with 26.8 kg $m^{-3}$ shown as bold.*

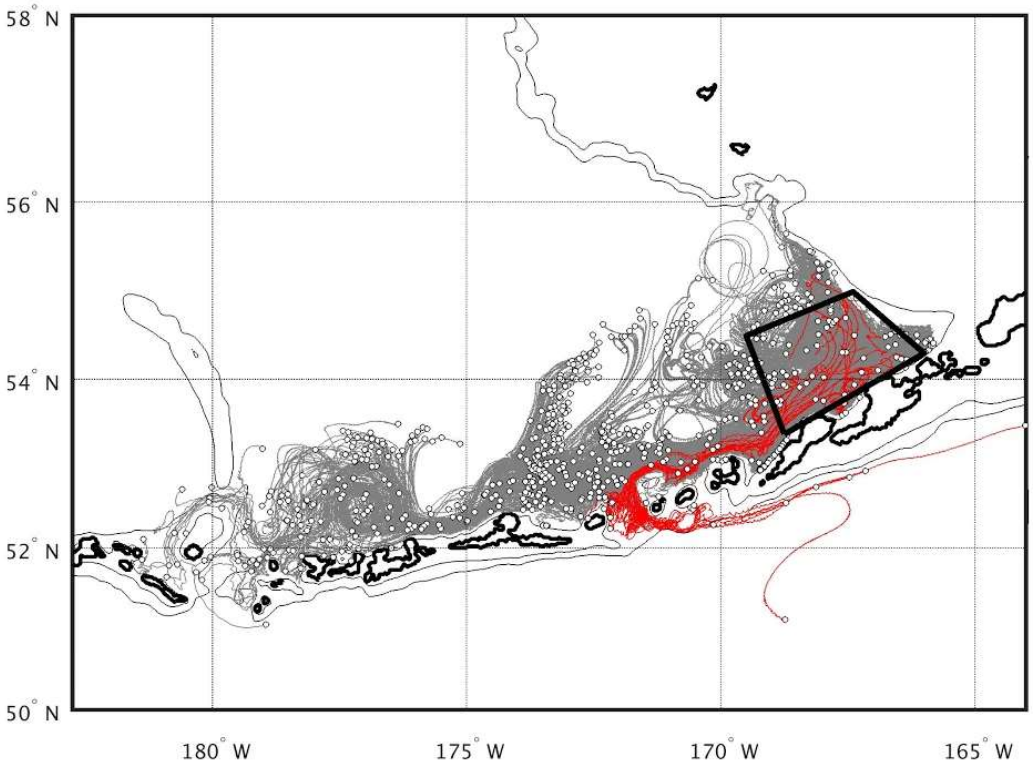


*Figure 12 Trajectories of the Lagrangian particles released in Bering Canyon (black box) on 26.8 kg $m^{-3}$isopycnal and tracked on the same isopycnal surface backwards for 106 days. End locations are shown as white circles. Red paths indicate trajectories of the particles that have traveled through Amukta Pass.*

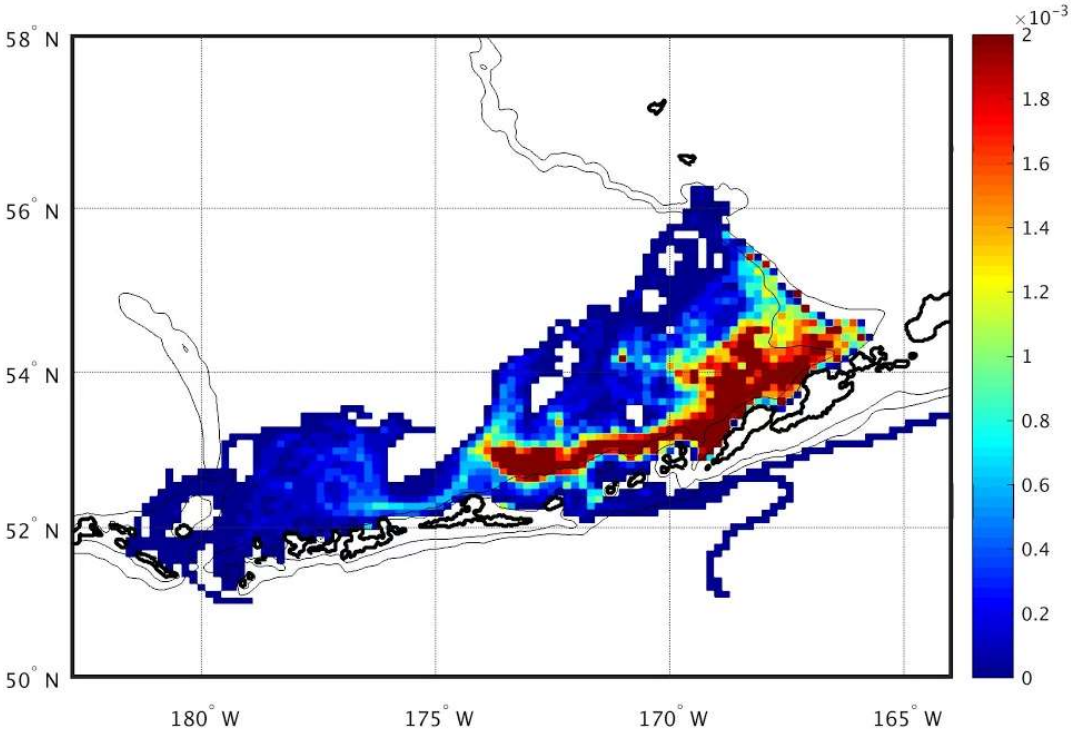


*Figure 13 PDF of particle positions on the 26.8 kg $m^{-3}$isopycnal, based on the results of the backward Lagrangian tracking.*

## 3. Minor Chapter: Forecast product and uncertainty quantification off the Oregon/Washington Coast

### 3.1 Introduction.

The Oregon Coast is located in the Pacific Northwest of the United States along the eastern boundary of the Pacific Ocean, where diverse marine resources support productive fisheries. Commercial fishing is culturally and economically important to coastal communities in Oregon, contributing more than $500 million annually in personal income [*ODFW*, 2017]. However, commercial fishermen regularly risk personal safety, property, and economic loss due to the hazards that arise from navigating the marine environment in the Pacific Northwest. Ocean conditions can become hazardous due to dynamic weather patterns and large storms that travel across the Pacific Ocean. This is particularly dangerous in the winter months when fishermen are most likely to be at sea harvesting Dungeness crab, the most valuable fishery in Oregon [*ODFW*, 2017]. The act of entering and leaving port, or "crossing the bar," is particularly hazardous in the Pacific Northwest due to the way coastal rivers meet the ocean. This complex interaction of the natural and human systems along the Oregon coast creates risks and uncertainties around the safety and economics of the commercial fishing fleet, as well as the forecasters' ability to predict the ocean conditions.

To cope with these risks, commercial fishermen regularly seek out sources of ocean condition information about temperatures, currents, waves, and wind to inform their decisions. In recent years, on a national level, researchers have brought forth integrated coastal observing and modelling systems that have substantially advanced the quality of coastal forecasts with the

recognized need to transform it into products that meet the data needs of the ocean use community [*Kourafalou et al.*, 2015]. To address these needs in Oregon, a research project was undertaken in the Marine Resource Management (MRM) graduate program at Oregon State University (OSU) to engage with members of the commercial fishing fleet in Newport, OR. The goal of this project was to make an effort to document and understand how fishermen make strategic decisions about ocean use [*Duncan*, 2014]. Findings revealed that the fishermen used a wide variety of data sources for multiple reasons, and lacked a single trusted source of information. This led to a collaborative effort that created seacast.org [*Seacast*, 2017], a web interface that presents ocean forecast data provided by marine OSU scientists A. Kurapov and S. Erofeeva in a simple and intuitive format driven by the needs of the fishermen. Today, *Seacast* [2017] continues to be used and improved based on feedback from local fishermen.

Forecasting tools and the models that inform them (such as *Seacast* [2017]) are subject to error due to the chaotic character of the atmosphere and the inevitable inadequacies in observations and computer models [*National Research Council*, 2006]. Uncertainty, while a fundamental characteristic of any forecast, is rarely reported or visualized in ocean condition forecasts. This is due to the nature of ocean forecasting being different than weather forecasting models. In typical weather forecasting methods, uncertainty is defined as a range of values wherein the "true" value exists. To derive this range of values, weather prediction often uses ensemble forecasting. This methodology produces a set of forecasts from slightly different initial conditions to result in a range of possible outcomes [*NOAA*, 2017]. Ocean condition forecasts utilized by Seacast use only one model forecast, called deterministic modelling. The OSU modeling group does not run an ensemble because of limitations in computational resources. In this type of modelling, there is no range of possible outcomes available for statistical analysis,

and thus no readily available measure of uncertainty. However, were these metrics available, the forecasting tool could potentially become more useful to data users during their decision-making process.

The different language and perceptions surrounding the definition of uncertainty complicate the communication of uncertainty between scientists and fishermen, which can lead to confusion and a lack of trust between the two parties. One way to overcome these differences in communication and to strengthen relationships is by understanding the underlying perceptions of risk and uncertainty towards the ocean and ocean forecasting for both communities. Web interfaces that deliver ocean condition forecast information, like *Seacast* [2017], serve as boundary objects that bring together different groups of people and bridge perceptual and practical differences in understanding [*Star and Griesemer*, 1989; *Karsten et al.*, 2001; *Leigh Star*, 2010; *Huvila et al.*, 2017]. Implementing this understanding can bridge the gap in communication through the creation of uncertainty metrics that serve as boundary objects for both parties. For scientists, this would mean the creation of metrics that are mathematically rigorous, and for data users, this would translate into uncertainty metrics that are consistent with their intuition and experience. These uncertainty metrics would therefore be comfortable for both parties. For the purposes of this report, the term 'uncertainty metrics' refers to model accuracy measurements which will be further described in the Methods and Results section. Communicating these metrics could ultimately serve to empower strategic decision-making based on each fisherman's unique situation and provide more objective and transparent forecasts with respect to the perceptions of each party.

In this report, we build off of the knowledge and relationships created from the Seacast tool [2017] to explore the perceptions of uncertainty for both data providers and users. We then

use the knowledge of these perceptions to derive metrics that address uncertainty which are acceptable to both parties. We developed the following research question in order to guide our work on this topic: 'How can ocean forecasts and their uncertainty be quantified and communicated to commercial fishermen?' To address this question and achieve these goals, the Ocean Condition Forecast (OCF) Team was formed in September of 2016 as part of the National Science Foundation Research Trainee (NRT) Fellowship in Risk and Uncertainty Quantification and Communication in Marine Science at OSU. It is composed of four graduate students that represent different facets of the ocean condition forecast process. This process includes the generation of forecasted data and associated uncertainty metrics, integration of uncertainty metrics into the Seacast platform, and assimilation of the divergent user or data provider perspectives into the entire process. The team members are the respective counterparts to this process and include two ocean modelers, one cartographer, and one social scientist. A transdisciplinary approach was used to generate the uncertainty metrics and communication design, as will be explained further in the following section.

## 3.2 Approach.

### *3.2.1 Transdisciplinary Process*

A transdisciplinary approach was used to guide OCF team members to inform and expand their disciplinary limitations and definitions of technical concepts, which ultimately resulted in a product that no one student could have achieved on their own. The societally-driven questions of how to create useful ocean condition forecasts and how to account for and represent the uncertainty of forecasts do not reside in a single disciplinary home, as the meaning of uncertainty

transcends disciplinary boundaries, professions, and problem domains [*Smithson*, 2008]. Transdisciplinary research is well suited to this problem because it goes beyond disciplinary boundaries and brings together researchers with varied expertise to address a problem they define under a joint conceptual framework [*Ciannelli et al.*, 2014]. This approach involved creating a clear framework for communication between the team members and cultivating strong relationships between them. Establishing this groundwork allows team members to collaborate more effectively [*Klein*, 2013; *Cheruvelil et al.*, 2014].

### *3.2.2 Defining Uncertainty*

The team's approach to defining uncertainty involves developing a quantification of ocean condition model uncertainty that is meaningful to both scientists and fishermen given the constraints of ocean condition forecasting. Uncertainty may be broadly defined as a situation in which a given event may result in more than one expected outcome. People make decisions in an effort to manage this uncertainty [*Pielke*, 2007]. Uncertainty associated with the creation, dissemination, and use of ocean condition forecasts has a strong influence on the decision-making process of fishermen, yet it is rarely expressed or reported as part of forecast products [*National Research Council*, 2003, 2006; *A.M.S. Council*, 2008]. The difficulty in expressing uncertainty in forecasts is due to the nature of uncertainty, which is such that there is no one universal definition. Some ways it can be expressed include: something that is known or known imprecisely, more than one possible outcome in a situation, or simply – doubt [*National Research Council*, 2006; *Pielke*, 2007; *BIPM et al.*, 2008]. Deriving one definition of uncertainty that satisfies data providers as well as data users poses challenges, in that each group

defines uncertainty differently. This has resulted in a lack of current standards for representing the uncertainty contained within ocean condition model output.

Ocean condition forecast providers think of uncertainty as a quantifiable number, such as a bias or a measure of variance [*Pielke*, 2007]. They derive this number from the uncertainty associated with deterministic ocean models. These uncertainties may consist of structural uncertainty, which refers to the underlying physics which govern model behavior, or parametric uncertainty, which refers to numerical model inputs [*Charles*, 1998]. This typically results in a metric of uncertainty that is quantified as a statistical distribution, or a range of values which can encompass the true value. In contrast, fishermen have a more tangible experience with uncertainty. For fishermen, uncertainty in the context of ocean conditions is strongly related to personal and financial risk. From their perspective, uncertainty is related to doubt. Doubt is associated with the accuracy of forecasts which, in turn, can complicate decision making. For fishermen, forecasts are predictions that they assign relative confidence to based on their intuition, which is derived from their experience with the ocean and using a variety of forecast tools.

### *3.2.3 Communicating Uncertainty in Ocean Forecasts*

The team's approach to communicating uncertainty related to ocean condition forecasts aims to use visualization techniques that are closely related to those that fishermen are already familiar with. The quantification of model uncertainty metrics must be paired with the communication of those metrics in a way that is clear and readily understood. Challenges arise when techniques for quantifying uncertainty are incompatible with the types of visualizations

that fishermen are accustomed to. For example, offshore buoys are effective for validating wave models at a coarse spatial resolution at specific locations, but it would be more useful to fishermen if the model could be validated at a finer resolution over the entire area in which they work. Ocean condition forecasts already serve as a platform for conveying information, and should be used for integrating new uncertainty metrics. While perfecting the form of this communication is outside the scope of this project, preliminary visualizations of the resulting uncertainty metrics were produced and these are described in the 'Methods and Results' section.

### 3.3 Model Setup.

Considering the stakeholder perspective on risk and uncertainty helped shape the efforts in quantifying the uncertainty in the surface current forecast. Commercial fishermen require their forecasts to be accurate to be useful, so quantifying a measure of accuracy would be most useful for this stakeholder group. Additionally, interactions with the stakeholders have revealed that commercial fishermen define model accuracy as how well the models represent observations. These revelations led to the use root mean square difference, or "error" (RMSE) as a metric for accuracy quantification, particularly for surface currents. Interests of the commercial fishermen also led us to use the ocean model to calculate new oceanic variables such as the depth of the thermocline.

These fields and metrics are computed using outputs of the OSU coastal ocean forecast system that uses a three-dimensional ocean circulation model and data assimilation. The model dynamics are based on the Regional Ocean Modeling System (ROMS, www.myroms.org). It uses terrain following vertical coordinates and advanced numerics [*Shchepetkin and McWilliams*,

2003, 2005]. Vertical, subgrid turbulence is parameterized using the Mellor-Yamada scheme [*Mellor and Yamada*, 1982].

The model domain spans 40˚ N to 50˚ N (middle of Vancouver Island) and 130˚ W to the U.S. West Coast. The model grid is a regular latitude-longitude grid with a horizontal resolution of about 2 km. 40 layers are used in the vertical. The surface and bottom boundary layers are relatively better resolved.

A bulk flux formulation is used to compute atmospheric forcing [*Fairall et al.*, 1996] which requires the following atmospheric fields: near surface wind speed and direction, air pressure, net shortwave radiation and downward longwave radiation, relative humidity, air temperature, and precipitation. These fields are obtained from the NOAA North American Mesoscale Model (NAM) that has a 12-km horizontal resolution; the fields are provided with the 3-hour temporal resolution. Freshwater discharges from the Columbia River, Fraser River, and 15 small rivers that enter the Puget Sound and Juan de Fuca Strait are included.

Open boundary conditions are obtained from the 1/12˚ degree resolution, U.S. Navy global data assimilation Hybrid Coordinate Ocean Model (HYCOM, www.hycom.org) [*Chassignet et al.*, 2007]. HYCOM provides instantaneous fields once a day. To avoid aliasing inertial motion and day to day noise that can be associated with the HYCOM adjustment to data assimilation correction, a 5-day half amplitude filter is applied to the HYCOM fields. Tides are added at open boundaries using the tidal sea level and the barotropic velocity amplitudes and phases for the eight most dominant tidal constituents ($M_2$, $S_2$, $N_2$, $K_2$, $O_1$, $K_1$, $P_1$, and $Q_1$) [*Egbert and Erofeeva*, 2002].

The OSU forecast system delivers daily updates of three-day forecasts of ocean currents, temperature and salinity. Once every three days data assimilation is run to correct the recent ocean state estimate and make it closer to the available observations of surface currents from a network of high frequency (HF) radars, sea surface temperature from the geostationary GOES satellite, and sea surface height from multiple different satellite altimetry missions. The data assimilation is done using the 4DVAR variational method in three-day time windows using tangent linear and adjoint codes developed at OSU [*Kurapov et al.*, 2009, 2011; *Yu et al.*, 2012].

## 3.4. Results.

### *3.4.1 New Forecast Products*

Providing a forecast of the thermocline depth for commercial fishermen required some inquiry to their definition of the thermocline. One way to define the thermocline is to find a location of maximum buoyancy frequency squared, given by $N^2 = \frac{g}{\rho_o}\frac{\partial \rho}{\partial z}$. Correspondence with the commercial fishermen revealed that they commonly define the thermocline as the depth in which the temperature is 2˚ F less than the surface temperature. Both of these methods were used to calculate and forecast the depth of the thermocline. In this calculation, daily averaged temperature and salinity were used in an effort to smooth potential inversions and remove false shallow depths.

Using the buoyancy frequency in this calculation can produce rapid changes in thermocline depth in the horizontal (Figure 14). The commercial fishermen's definition yields a smoother forecasted field. In well-mixed, shallow waters where the temperature change over the

entire water column is < 2˚ F it may not produce a number (Figure 15). Both of these methods produce relatively similar results with difference in depth rarely exceeding 10 m.

### *3.4.2 Uncertainty Quantification*

As a part of their the individual research, the social scientist conducted interviews with commercial fishermen. As an exploratory measure, the researcher set up an individual "read through" session with each of the three members of the OCF team. The purpose of the "read through" was to provide insight to the team about the kind of information gained during the interviews, while simultaneously informing the social science researcher about what kinds of information were interesting and useful to the OCF team. In one such session it was revealed that commercial fishermen often think about model uncertainty in terms of how accurately the model represents in-situ or their own observations. In an effort to recreate this thought process, root mean square error (RMSE) was chosen as the uncertainty metric to evaluate surface currents provided by the model. Due to availability of the model data and preferences of the commercial fishermen, this calculation will be performed for the past 30 days of each forecast. The forecasts in this study span June 27 to July 31, 2017. It should be noted that the commercial fishermen like for this evaluation to be performed over the past 7 days or shorter, but RMSE on such a short time scale may not make sense mathematically.

RMSE is calculated by comparing model surface currents to high frequency (HF) radar observations available throughout the study time period. The HF radar data used here is available as hourly fields with two velocity components: u (meridional) and v (zonal) on a regular 6 km grid. The area encompassed by this data varies from day to day due to changing environmental

conditions. Model surface currents, provided every 2 hours, are sampled at times and locations when the HF radar data is available for 1, 2, and 3-day forecasts. Area averaged u and v velocity components for each forecast horizon (Figure 16, 17, and 18) qualitatively reproduce the data well, with the overall error increasing with forecast length. The model appears to do better at the beginning of July for all forecasts, and there is less error in the cross-shore (u) velocity than along-shore (v).

To spatially evaluate sources of greater error, RMSE was calculated at each model point where HF radar data was available for each forecast (Figure 19). Each forecast shows a similar spatial error structure. The model does better north of about 43.5˚ N where ensemble-based model predictability is generally better [*Kim et al.*, 2009]. There is also a noticeable source of error near the Columbia River estuary (just north of 46 ˚ N). The source of this error resides in both the alongshore and cross-shore components of velocity (Figure 20, 21). Note that the model does not have enough resolution to represent energetic outflows from the river mouth on the ebb tides. At the same time, HF radar current estimates are in error when the current speed is close to the wave speed (which would be close to 2 m/s in the river mouth). South of about 43.5˚ N the model does relatively worse than the rest of the domain, particularly south of 42˚ N. This error is a result of roughly equal contribution from the along-shore and cross-shore velocity components and is associated with the nonlinearities in the flow such as coastal jet separation at Cape Blanco and eddy formation in the coastal transition zone [*Koch et al.*, 2010]. In general, the error is larger with longer forecasts (Figure 19, 20, 21).

It is important to note the lack of spatial coverage of the HF radar as limiting factor for evaluating surface currents west of 126˚ W and north of 46˚ N. While there is adequate data for a meaningful nearshore calculation on the Oregon Coast, there is a noticeable lack of data for the

northern half of Washington. This could prove to be frustrating for commercial fishermen in that area, and should be considered for future studies. The encouraging news is that the Northwest Association of Networked Ocean Observing Systems (www.nanoos.org) is providing funding this year to extend the HF radar network into Washington.

### 3.4. Summary.

As part of the NRT project, we tested new products for the fishermen, such as the thermocline depth forecast, and provided uncertainty quantification for the surface currents using RMSE calculation as an uncertainty metric. Interviews with commercial fishermen, conducted by the social scientist member of the OCF team, were used to guide the forecast and uncertainty desires of the stakeholders. The thermocline depth was forecasted using the buoyancy frequency and a definition ascertained from the commercial fishermen (2˚ F difference from the surface temperature). This forecast can be updated daily with the rest of the model output fields. RMSE for the area averaged velocity and at each location where HF radar data was available showing sources of error near the southern boundary of the model domain and near the Columbia River estuary. Model error also increases with longer forecasts. At the moment, surface currents are the only oceanic metric in this model tested for future use with Seacast.

While this study provides a strong start in the effort to quantify ocean forecasts and their uncertainty to commercial fishermen, there is plenty of future work to be done. Continued correspondence with the stakeholder group is necessary to ensure that forecasts remain useful and intuitive to the end users. There are opportunities to develop forecast products for the benefit of crabbers, such as the probability that the crab pot buoys can be seen on the water surface when

the fishermen come to retrieve those. One could potentially forecast whether or not the marker buoy is underwater using model output currents. Finally, our uncertainty quantification only covers a fraction of the model state vector. While this metric is still meaningful, continued research in uncertainty quantification outside the range of HF radar used for validation would be beneficial to commercial fishermen.

**3.6 References.**

A.M.S. Council (2008), Enhancing weather information with probability forecasts, in *Bulletin of the American Meteorological Society, 89*, pp. 1049–1053.

BIPM, I., I. IFCC, I. IUPAC, and O. ISO (2008), Evaluation of measurement data-guide for the expression of uncertainty in measurement, p. 167, Citado en las.

Charles, A. T. (1998), Living with uncertainty in fisheries: analytical methods, management priorities and the Canadian groundfishery experience, *Fisheries Research*, *37*(1), 37–50, doi:10.1016/S0165-7836(98)00125-8.

Chassignet, E. P., H. E. Hurlburt, O. M. Smedstad, G. R. Halliwell, P. J. Hogan, A. J. Wallcraft, R. Baraille, and R. Bleck (2007), The HYCOM (HYbrid Coordinate Ocean Model) data assimilative system, *Journal of Marine Systems*, *65*(1–4), 60–83, doi:10.1016/j.jmarsys.2005.09.016.

Cheruvelil, K. S., P. A. Soranno, K. C. Weathers, P. C. Hanson, S. J. Goring, C. T. Filstrup, and E. K. Read (2014), Creating and maintaining high-performing collaborative research teams: the importance of diversity and interpersonal skills, *Frontiers in Ecology and the Environment*, *12*(1), 31–38, doi:10.1890/130001.

Ciannelli, L. et al. (2014), Transdisciplinary graduate education in marine resource science and management, *ICES J Mar Sci*, *71*(5), 1047–1051, doi:10.1093/icesjms/fsu067.

Duncan, C. (2014), Cooperative product development between researchers and commercial fishermen to find applications for ocean condition forecasting, Unpublished Master's Thesis, Oregon State University, Corvallis, OR.

Egbert, G. D., and S. Y. Erofeeva (2002), Efficient Inverse Modeling of Barotropic Ocean Tides, *J. Atmos. Oceanic Technol.*, *19*(2), 183–204, doi:10.1175/1520-0426(2002)019<0183:EIMOBO>2.0.CO;2.

Fairall, C. W., E. F. Bradley, D. P. Rogers, J. B. Edson, and G. S. Young (1996), Bulk parameterization of air-sea fluxes for Tropical Ocean-Global Atmosphere Coupled-Ocean

Atmosphere Response Experiment, *Journal of Geophysical Research: Oceans*, *101*(C2), 3747–3764, doi:10.1029/95JC03205.

Huvila, I., T. D. Anderson, E. H. Jansen, P. McKenzie, and A. Worrall (2017), Boundary objects in information science, *Journal of the Association for Information Science and Technology*, *68*(8), 1807–1822, doi:10.1002/asi.23817.

Karsten, H., K. Lyytinen, M. Hurskainen, and T. Koskelainen (2001), Crossing boundaries and conscripting participation: representing and integrating knowledge in a paper machinery project, *Eur J Inf Syst*, *10*(2), 89–98, doi:10.1057/palgrave.ejis.3000395.

Kim, S., R. M. Samelson, and C. Snyder (2009), Ensemble-Based Estimates of the Predictability of Wind-Driven Coastal Ocean Flow over Topography, *Monthly Weather Review*, *137*(8), 2515–2537, doi:10.1175/2009MWR2631.1.

Klein, J. T. (2013), Communication and Collaboration in Interdisciplinary Research, in *Enhancing Communication & Collaboration in Interdisciplinary Research*, edited by M. O'Rourke, S. Crowley, S. D. Eigenbrode, and J. D. Wulfhorst, pp. 11–30.

Koch, A. O., A. L. Kurapov, and J. S. Allen (2010), Near-surface dynamics of a separated jet in the coastal transition zone off Oregon, *Journal of Geophysical Research*, *115*(C8), doi:10.1029/2009JC005704.

Kourafalou, V. H. et al. (2015), Coastal Ocean Forecasting: science foundation and user benefits, *Journal of Operational Oceanography*, *8*(sup1), s147–s167, doi:10.1080/1755876X.2015.1022348.

Kurapov, A. L., G. D. Egbert, J. S. Allen, and R. N. Miller (2009), Representer-based analyses in the coastal upwelling system, *Dynamics of Atmospheres and Oceans*, *48*(1–3), 198–218, doi:10.1016/j.dynatmoce.2008.09.002.

Kurapov, A. L., D. Foley, P. T. Strub, G. D. Egbert, and J. S. Allen (2011), Variational assimilation of satellite observations in a coastal ocean model off Oregon, *Journal of Geophysical Research*, *116*(C5), doi:10.1029/2010JC006909.

Leigh Star, S. (2010), This is Not a Boundary Object: Reflections on the Origin of a Concept, *Science, Technology, & Human Values*, *35*(5), 601–617, doi:10.1177/0162243910377624.

Mellor, G. L., and T. Yamada (1982), Development of a turbulence closure model for geophysical fluid problems, *Rev. Geophys.*, *20*(4), 851–875, doi:10.1029/RG020i004p00851.

Morss, R. E., J. L. Demuth, and J. K. Lazo (2008), Communicating Uncertainty in Weather Forecasts: A Survey of the U.S. Public, *Wea. Forecasting*, *23*(5), 974–991, doi:10.1175/2008WAF2007088.1.

National Research Council (2003), *Communicating Uncertainties in Weather and Climate Information: A Workshop Summary*, National Academies Press.

National Research Council (2006), *Completing the Forecast: Characterizing and Communicating Uncertainty for Better Decisions Using Weather and Climate Forecasts*, National Academies Press.

NOAA (2017), Global Ensemble Forecast System (GEFS) | National Centers for Environmental Information (NCEI) formerly known as National Climatic Data Center (NCDC), Available from: https://www.ncdc.noaa.gov/data-access/model-data/model-datasets/global-ensemble-forecast-system-gefs (Accessed 31 August 2017)

ODFW (2017), Oregon's Ocean Commercial Fisheries, Available from: http://www.dfw.state.or.us/mrp/docs/Backgrounder_Comm_Fishing.pdf (Accessed 31 August 2017)

Pielke, R. A. (2007), *The Honest Broker: Making Sense of Science in Policy and Politics*, Cambridge University Press.

Seacast (2017), Seacast, Available from: http://seacast.org/ (Accessed 31 August 2017)

Shchepetkin, A. F., and J. C. McWilliams (2003), A method for computing horizontal pressure-gradient force in an oceanic model with a nonaligned vertical coordinate, *J. Geophys. Res.*, *108*(C3), 3090, doi:10.1029/2001JC001047.

Shchepetkin, A. F., and J. C. McWilliams (2005), The regional oceanic modeling system (ROMS): a split-explicit, free-surface, topography-following-coordinate oceanic model, *Ocean Modelling*, *9*(4), 347–404, doi:10.1016/j.ocemod.2004.08.002.

Smithson, M. (2008), The many faces and masks of uncertainty, in *Uncertainty and Risk: Multidisciplinary Perspectives*, pp. 13–25.

Star, S. L., and J. R. Griesemer (1989), Institutional Ecology, `Translations' and Boundary Objects: Amateurs and Professionals in Berkeley's Museum of Vertebrate Zoology, 1907-39, *Soc Stud Sci*, *19*(3), 387–420, doi:10.1177/030631289019003001.

Yu, P., A. L. Kurapov, G. D. Egbert, J. S. Allen, and P. M. Kosro (2012), Variational assimilation of HF radar surface currents in a coastal ocean model off Oregon, *Ocean Modelling*, *49–50*, 86–104, doi:10.1016/j.ocemod.2012.03.001.

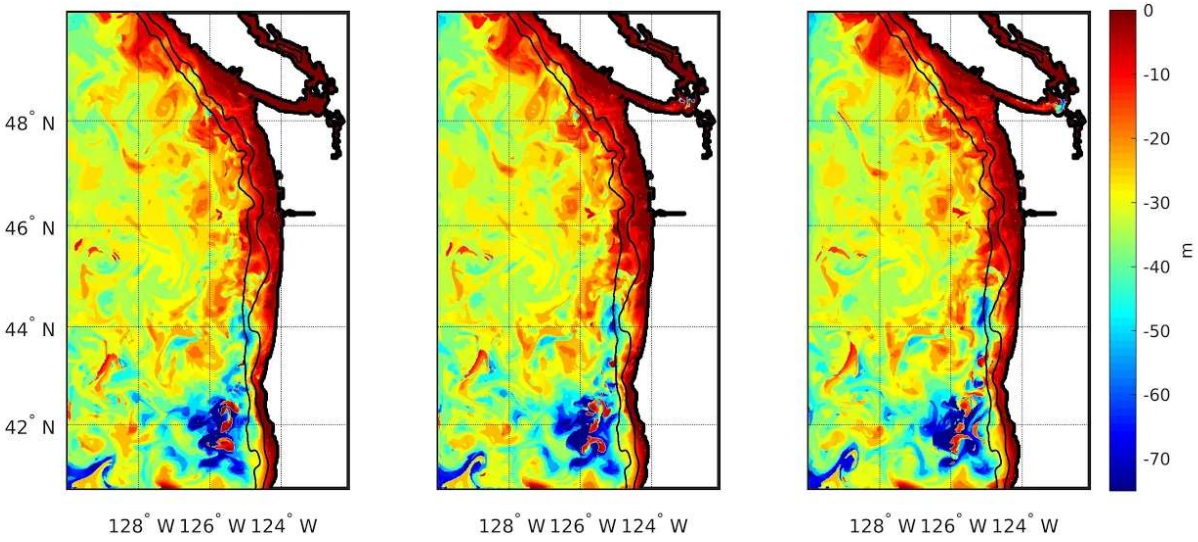


*Figure 14 Depth of the thermocline calculated using N2 with the 200 and 1000 m isobaths contoured (black) for forecast horizons of 1 day (left) [for August 22, 2017], 2 days (middle) [for August 23, 2017], and 3 days (right) [for August 24, 2017].*

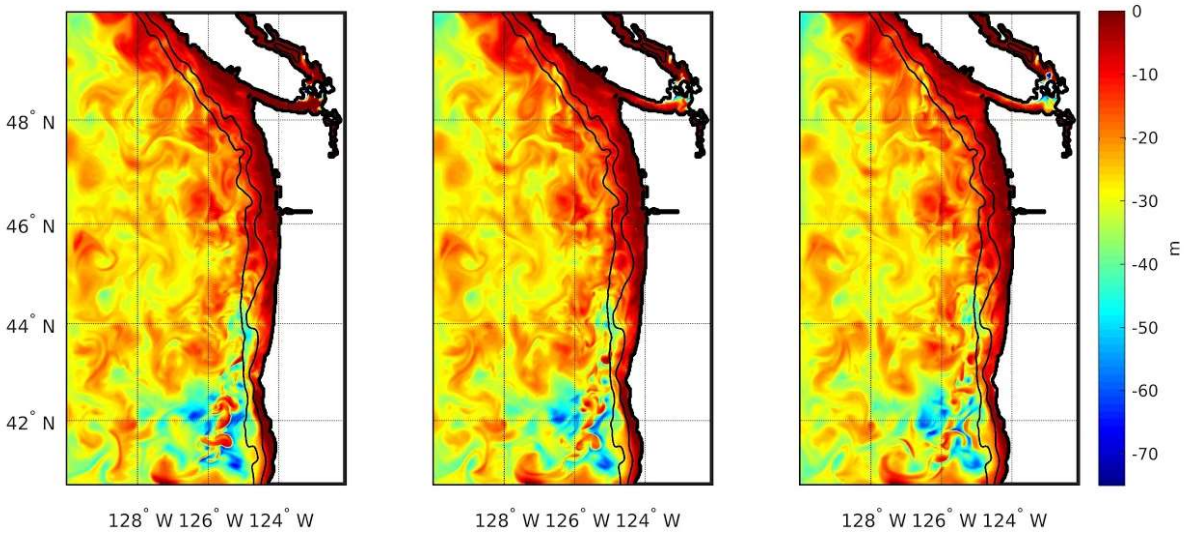


*Figure 15 Depth of the layer of 2˚F difference from the surface with the 200 and 1000 m isobaths contoured (black) for forecast horizons of 1 day (left) [for August 22, 2017], 2 days (middle) [for August 23, 2017], and 3 days (right) [for August 24, 2017].*

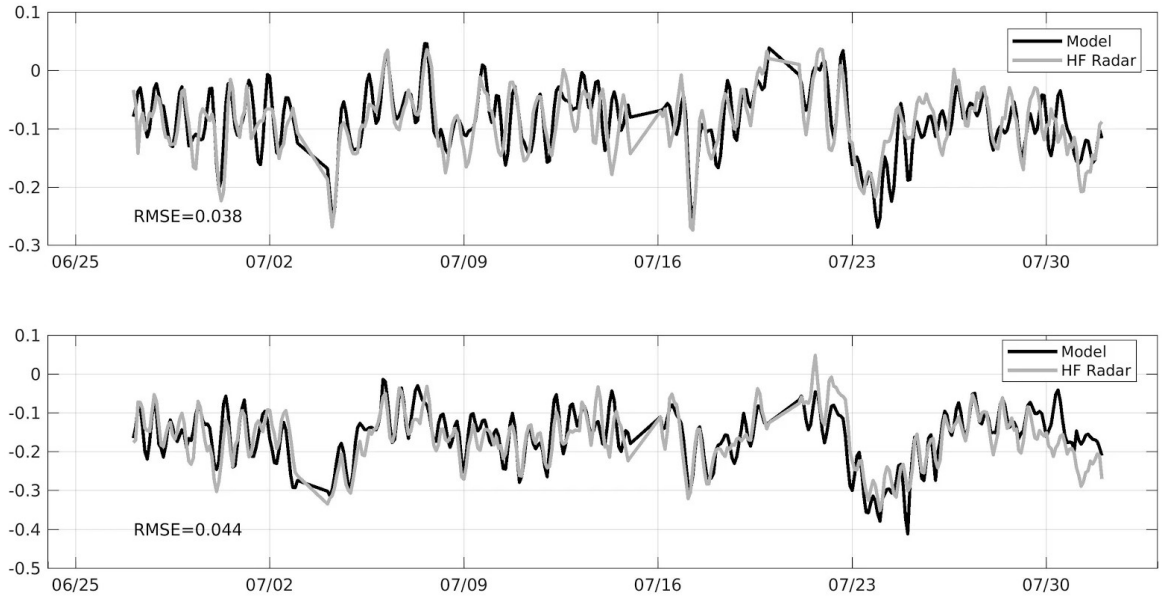


*Figure 16 1-day forecasts of area averaged instantaneous velocity for u (top) and v (bottom) velocity components for both the model (black) and HF Radar (gray).*

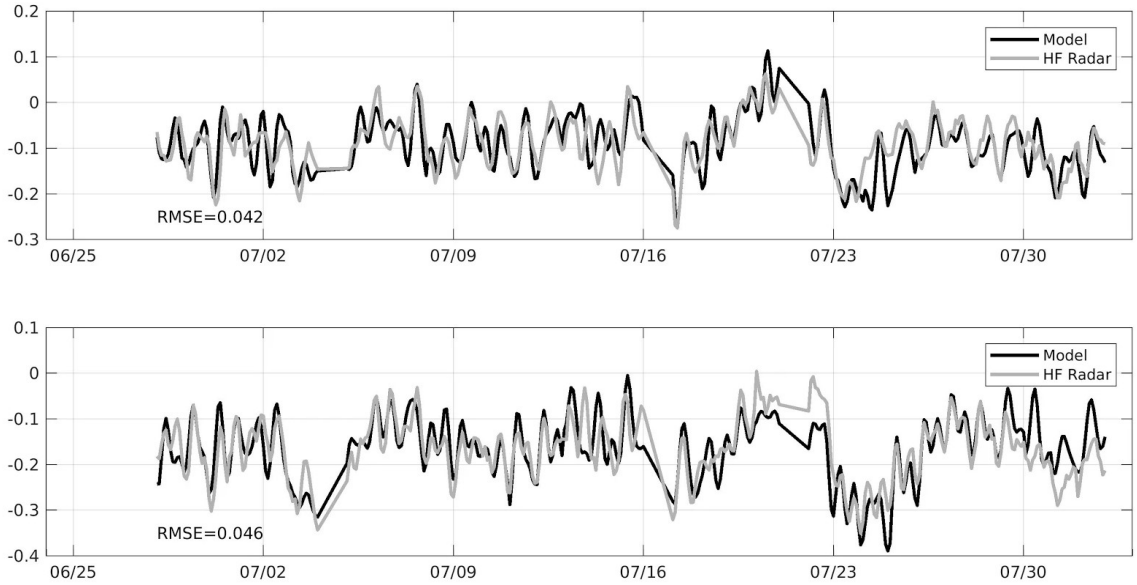


*Figure 17 2-day forecasts of area averaged instantaneous velocity for u (top) and v (bottom) velocity components for both the model (black) and HF Radar (gray).*

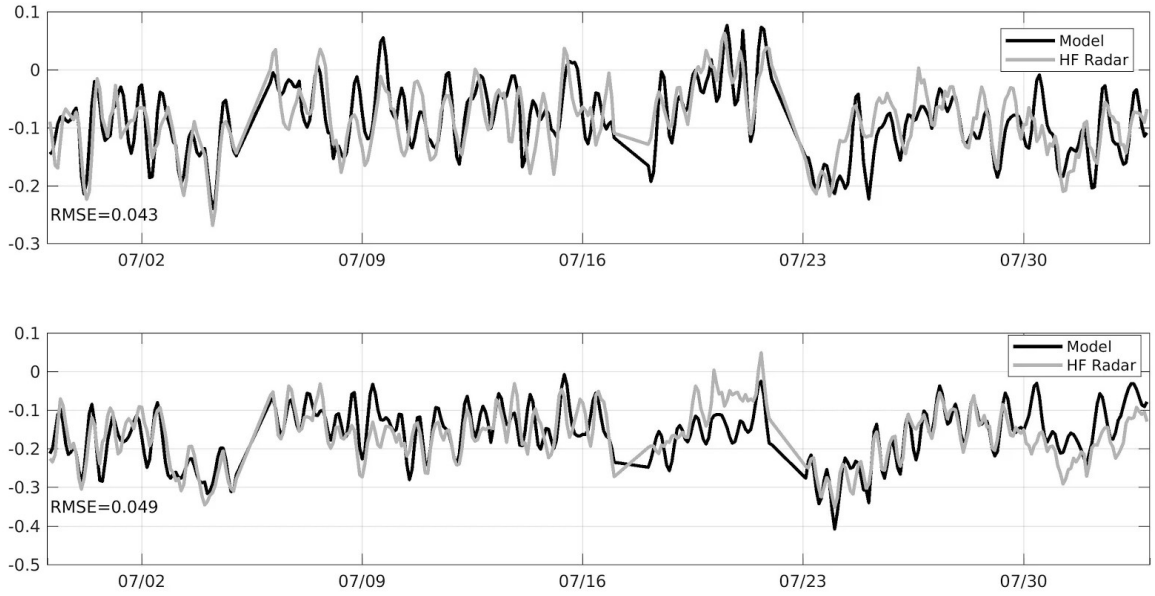


*Figure 18 3-day forecasts of area averaged instantaneous velocity for u (top) and v (bottom) velocity components for both the model (black) and HF Radar (gray).*

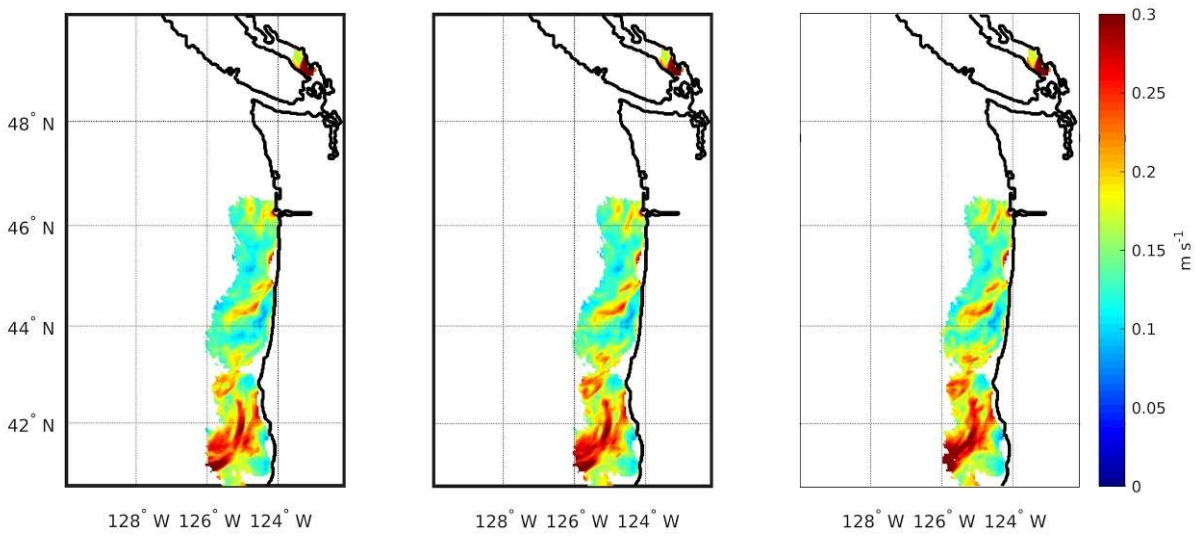


*Figure 19 RMSE of model output surface current speed and HF radar from June 27-July 31, 2017 for 1 (left), 2 (middle), and 3-day (right) forecasts.*

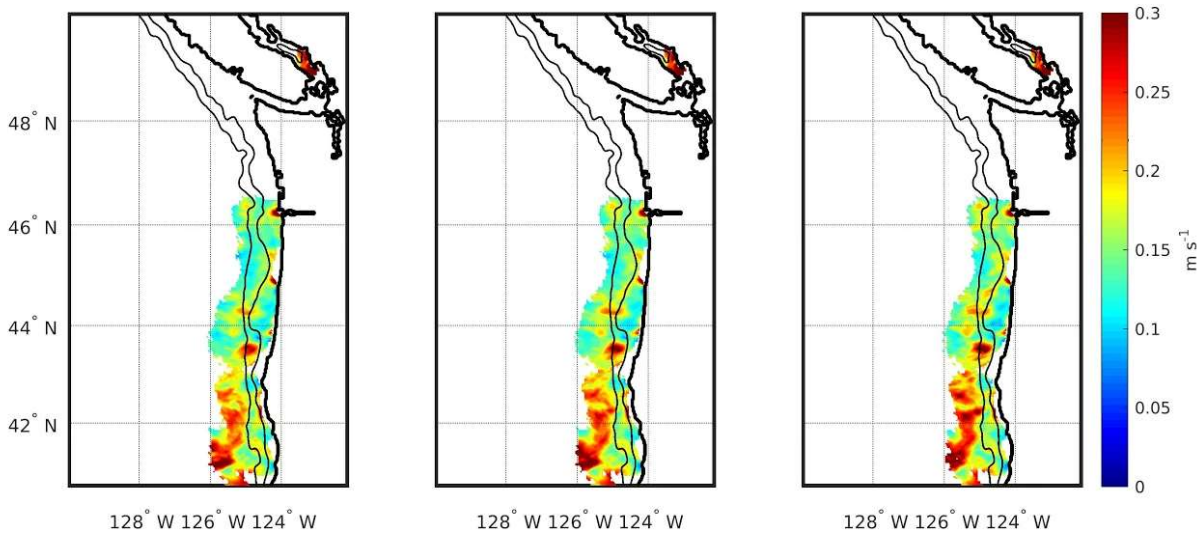


*Figure 20 RMSE of model output surface cross-shore current speed and HF radar from June 27-July 31, 2017 for 1 (left), 2 (middle), and 3-day (right) forecasts.*

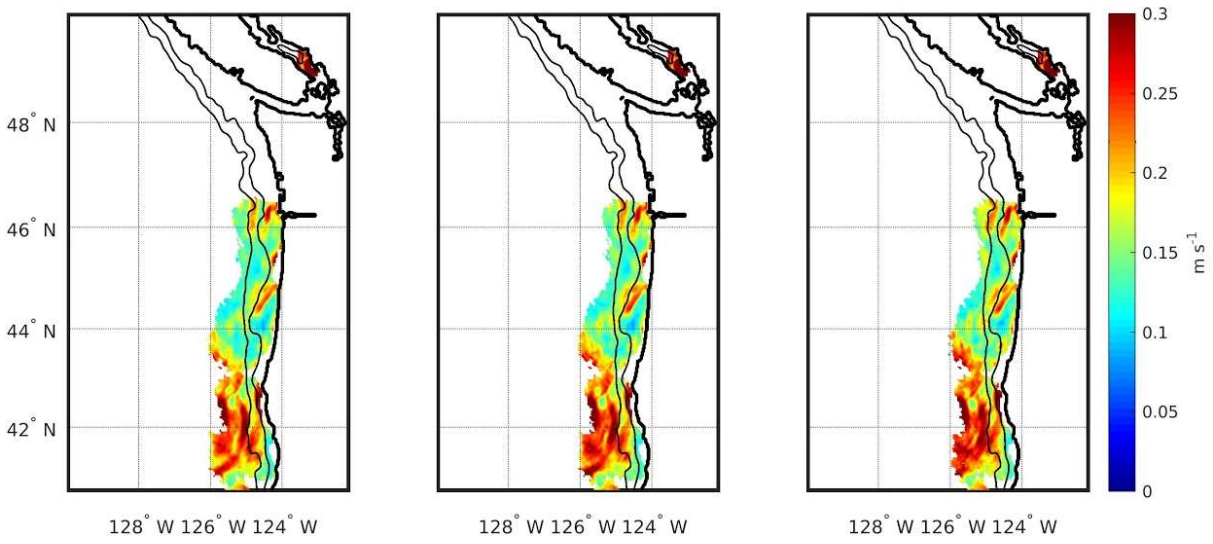


*Figure 21 RMSE of model output surface along-shore current speed and HF radar from June 27-July 31, 2017 for 1 (left), 2 (middle), and 3-day (right) forecasts.*

**Bibliography**

A.M.S. Council (2008), Enhancing weather information with probability forecasts, in *Bulletin of the American Meteorological Society, 89*, pp. 1049–1053.

Argo (2000), Argo float data and metadata from Global Data Assembly Centre (Argo GDAC), , doi:10.17882/42182.

BIPM, I., I. IFCC, I. IUPAC, and O. ISO (2008), Evaluation of measurement data-guide for the expression of uncertainty in measurement, p. 167, Citado en las.

Capet, X., J. C. McWilliams, M. J. Molemaker, and A. F. Shchepetkin (2008), Mesoscale to Submesoscale Transition in the California Current System. Part I: Flow Structure, Eddy Flux, and Observational Tests, *J. Phys. Oceanogr.*, *38*(1), 29–43, doi:10.1175/2007JPO3671.1.

Chapman, D. C. (1985), Numerical Treatment of Cross-Shelf Open Boundaries in a Barotropic Coastal Ocean Model, *J. Phys. Oceanogr.*, *15*(8), 1060–1075, doi:10.1175/1520-0485(1985)015<1060:NTOCSO>2.0.CO;2.

Charles, A. T. (1998), Living with uncertainty in fisheries: analytical methods, management priorities and the Canadian groundfishery experience, *Fisheries Research*, *37*(1), 37–50, doi:10.1016/S0165-7836(98)00125-8.

Chassignet, E. P., H. E. Hurlburt, O. M. Smedstad, G. R. Halliwell, P. J. Hogan, A. J. Wallcraft, R. Baraille, and R. Bleck (2007), The HYCOM (HYbrid Coordinate Ocean Model) data assimilative system, *Journal of Marine Systems*, *65*(1–4), 60–83, doi:10.1016/j.jmarsys.2005.09.016.

Chelton, D. B., R. A. deSzoeke, M. G. Schlax, K. El Naggar, and N. Siwertz (1998), Geographical Variability of the First Baroclinic Rossby Radius of Deformation, *J. Phys. Oceanogr.*, *28*(3), 433–460, doi:10.1175/1520-0485(1998)028<0433:GVOTFB>2.0.CO;2.

Cheruvelil, K. S., P. A. Soranno, K. C. Weathers, P. C. Hanson, S. J. Goring, C. T. Filstrup, and E. K. Read (2014), Creating and maintaining high-performing collaborative research teams: the importance of diversity and interpersonal skills, *Frontiers in Ecology and the Environment*, *12*(1), 31–38, doi:10.1890/130001.

Ciannelli, L. et al. (2014), Transdisciplinary graduate education in marine resource science and management, *ICES J Mar Sci*, *71*(5), 1047–1051, doi:10.1093/icesjms/fsu067.

Clement, J. L., W. Maslowski, L. W. Cooper, J. M. Grebmeier, and W. Walczowski (2005), Ocean circulation and exchanges through the northern Bering Sea—1979–2001 model results, *Deep Sea Research Part II: Topical Studies in Oceanography*, *52*(24), 3509–3540, doi:10.1016/j.dsr2.2005.09.010.

Clement Kinney, J., and W. Maslowski (2012), On the oceanic communication between the Western Subarctic Gyre and the deep Bering Sea, *Deep Sea Research Part I: Oceanographic Research Papers*, *66*, 11–25, doi:10.1016/j.dsr.2012.04.001.

Clement Kinney, J., W. Maslowski, and S. Okkonen (2009), On the processes controlling shelf–basin exchange and outer shelf dynamics in the Bering Sea, *Deep Sea Research Part II: Topical Studies in Oceanography*, *56*(17), 1351–1362, doi:10.1016/j.dsr2.2008.10.023.

Danielson, S., E. Curchitser, K. Hedstrom, T. Weingartner, and P. Stabeno (2011), On ocean and sea ice modes of variability in the Bering Sea, *J. Geophys. Res.*, *116*(C12), C12034, doi:10.1029/2011JC007389.

Danielson, S., T. Weingartner, K. Aagaard, J. Zhang, and R. Woodgate (2012), Circulation on the central Bering Sea shelf, July 2008 to July 2010, *J. Geophys. Res.*, *117*(C10), C10003, doi:10.1029/2012JC008303.

Danielson, S. L., T. J. Weingartner, K. S. Hedstrom, K. Aagaard, R. Woodgate, E. Curchitser, and P. J. Stabeno (2014), Coupled wind-forced controls of the Bering–Chukchi shelf circulation and the Bering Strait throughflow: Ekman transport, continental shelf waves, and variations of the Pacific–Arctic sea surface height gradient, *Progress in Oceanography*, *125*, 40–61, doi:10.1016/j.pocean.2014.04.006.

Donlon, C. J., M. Martin, J. Stark, J. Roberts-Jones, E. Fiedler, and W. Wimmer (2012), The Operational Sea Surface Temperature and Sea Ice Analysis (OSTIA) system, *Remote Sensing of Environment*, *116*, 140–158, doi:10.1016/j.rse.2010.10.017.

Duncan, C. (2014), Cooperative product development between researchers and commercial fishermen to find applications for ocean condition forecasting, Unpublished Master's Thesis, Oregon State University, Corvallis, OR.

Durski, S., A. Kurapov, J. Zhang, and G. Panteleev (2015), Circulation in the Eastern Bering Sea: Inferences from a 2-km-resolution model, *ResearchGate*, doi:http://dx.doi.org/10.1016/j.dsr2.2015.02.002.

Egbert, G. D., and S. Y. Erofeeva (2002), Efficient Inverse Modeling of Barotropic Ocean Tides, *J. Atmos. Oceanic Technol.*, *19*(2), 183–204, doi:10.1175/1520-0426(2002)019<0183:EIMOBO>2.0.CO;2.

Ezer, T., and L.-Y. Oey (2010), The Role of the Alaskan Stream in Modulating the Bering Sea Climate, *Journal of Geophysical Research: Oceans*, doi:10.1029/2009jc005830.

Fairall, C. W., E. F. Bradley, D. P. Rogers, J. B. Edson, and G. S. Young (1996), Bulk parameterization of air-sea fluxes for Tropical Ocean-Global Atmosphere Coupled-Ocean Atmosphere Response Experiment, *Journal of Geophysical Research: Oceans*, *101*(C2), 3747–3764, doi:10.1029/95JC03205.

Fairall, C. W., E. F. Bradley, J. E. Hare, A. A. Grachev, and J. B. Edson (2003), Bulk Parameterization of Air–Sea Fluxes: Updates and Verification for the COARE Algorithm, *J. Climate*, *16*(4), 571–591, doi:10.1175/1520-0442(2003)016<0571:BPOASF>2.0.CO;2.

Favorite, F. (1974), Flow into the Bering Sea through Aleutian island passes, in *Oceanography of the Bering Sea With Emphasis on Renewable Resources*, edited by D. W. Hood and E. J. Kelley, pp. 3–37, Institute of Marine Science, University of Alaska, Fairbanks, Alaska.

Flather, R. A. (1976), *A tidal model of the north-west European continental shelf*.

Foreman, M. G. G., P. F. Cummins, J. Y. Cherniawsky, and P. Stabeno (2006), Tidal energy in the Bering Sea, *Journal of Marine Research*, *64*(6), 797–818, doi:10.1357/002224006779698341.

Hu, H., and J. Wang (2010), Modeling effects of tidal and wave mixing on circulation and thermohaline structures in the Bering Sea: Process studies, *J. Geophys. Res.*, *115*(C1), C01006, doi:10.1029/2008JC005175.

Hunt, G. L., P. J. Stabeno, S. Strom, and J. M. Napp (2008), Patterns of spatial and temporal variation in the marine ecosystem of the southeastern Bering Sea, with special reference to the Pribilof Domain, *Deep Sea Research Part II: Topical Studies in Oceanography*, *55*(16), 1919–1944, doi:10.1016/j.dsr2.2008.04.032.

Huvila, I., T. D. Anderson, E. H. Jansen, P. McKenzie, and A. Worrall (2017), Boundary objects in information science, *Journal of the Association for Information Science and Technology*, *68*(8), 1807–1822, doi:10.1002/asi.23817.

Johnson, G. C., P. J. Stabeno, and S. C. Riser (2004), The Bering Slope Current System Revisited*, *J. Phys. Oceanogr.*, *34*(2), 384–398, doi:10.1175/1520-0485(2004)034<0384:TBSCSR>2.0.CO;2.

Kantha, L. H., and C. A. Clayson (1994), An improved mixed layer model for geophysical applications, *J. Geophys. Res.*, *99*(C12), 25235–25266, doi:10.1029/94JC02257.

Karsten, H., K. Lyytinen, M. Hurskainen, and T. Koskelainen (2001), Crossing boundaries and conscripting participation: representing and integrating knowledge in a paper machinery project, *Eur J Inf Syst*, *10*(2), 89–98, doi:10.1057/palgrave.ejis.3000395.

Kim, S., R. M. Samelson, and C. Snyder (2009), Ensemble-Based Estimates of the Predictability of Wind-Driven Coastal Ocean Flow over Topography, *Monthly Weather Review*, *137*(8), 2515–2537, doi:10.1175/2009MWR2631.1.

Klein, J. T. (2013), Communication and Collaboration in Interdisciplinary Research, in *Enhancing Communication & Collaboration in Interdisciplinary Research*, edited by M. O'Rourke, S. Crowley, S. D. Eigenbrode, and J. D. Wulfhorst, pp. 11–30.

Koch, A. O., A. L. Kurapov, and J. S. Allen (2010), Near-surface dynamics of a separated jet in the coastal transition zone off Oregon, *Journal of Geophysical Research*, *115*(C8), doi:10.1029/2009JC005704.

Kourafalou, V. H. et al. (2015), Coastal Ocean Forecasting: science foundation and user benefits, *Journal of Operational Oceanography*, *8*(sup1), s147–s167, doi:10.1080/1755876X.2015.1022348.

Kowalik, Z. (1999), Bering Sea tides, in *Dynamics of the Bering Sea*, edited by T. R. Loughlin and K. Ohtani, pp. 93–127, University of Alaska Sea Grant, Fairbanks, Alaska.

Kurapov, A. L., G. D. Egbert, J. S. Allen, and R. N. Miller (2009), Representer-based analyses in the coastal upwelling system, *Dynamics of Atmospheres and Oceans*, *48*(1–3), 198–218, doi:10.1016/j.dynatmoce.2008.09.002.

Kurapov, A. L., D. Foley, P. T. Strub, G. D. Egbert, and J. S. Allen (2011), Variational assimilation of satellite observations in a coastal ocean model off Oregon, *Journal of Geophysical Research*, *116*(C5), doi:10.1029/2010JC006909.

Ladd, C. (2014), Seasonal and interannual variability of the Bering Slope Current, *Deep Sea Research Part II: Topical Studies in Oceanography*, *109*, 5–13, doi:10.1016/j.dsr2.2013.12.005.

Leigh Star, S. (2010), This is Not a Boundary Object: Reflections on the Origin of a Concept, *Science, Technology, & Human Values*, *35*(5), 601–617, doi:10.1177/0162243910377624.

Li, L., A. J. Miller, J. L. McClean, I. Eisenman, and M. C. Hendershott (2014), Processes driving sea ice variability in the Bering Sea in an eddying ocean/sea ice model: anomalies from the mean seasonal cycle, *Ocean Dynamics*, *64*(12), 1693–1717, doi:10.1007/s10236-014-0769-7.

Mellor, G. L., and T. Yamada (1982), Development of a turbulence closure model for geophysical fluid problems, *Rev. Geophys.*, *20*(4), 851–875, doi:10.1029/RG020i004p00851.

Mesinger, F. et al. (2006), North American Regional Reanalysis, *Bull. Amer. Meteor. Soc.*, *87*(3), 343–360, doi:10.1175/BAMS-87-3-343.

Molemaker, M. J., J. C. McWilliams, and W. K. Dewar (2014), Submesoscale Instability and Generation of Mesoscale Anticyclones near a Separation of the California Undercurrent, *J. Phys. Oceanogr.*, *45*(3), 613–629, doi:10.1175/JPO-D-13-0225.1.

Morss, R. E., J. L. Demuth, and J. K. Lazo (2008), Communicating Uncertainty in Weather Forecasts: A Survey of the U.S. Public, *Wea. Forecasting*, *23*(5), 974–991, doi:10.1175/2008WAF2007088.1.

Nakamura, T., Y. Isoda, H. Mitsudera, S. Takagi, and M. Nagasawa (2010), Breaking of unsteady lee waves generated by diurnal tides, *Geophys. Res. Lett.*, *37*(4), L04602, doi:10.1029/2009GL041456.

National Research Council (2003), *Communicating Uncertainties in Weather and Climate Information: A Workshop Summary*, National Academies Press.

National Research Council (2006), *Completing the Forecast: Characterizing and Communicating Uncertainty for Better Decisions Using Weather and Climate Forecasts*, National Academies Press.

NOAA (2017), Global Ensemble Forecast System (GEFS) | National Centers for Environmental Information (NCEI) formerly known as National Climatic Data Center (NCDC), Available from: https://www.ncdc.noaa.gov/data-access/model-data/model-datasets/global-ensemble-forecast-system-gefs (Accessed 31 August 2017)

ODFW (2017), Oregon's Ocean Commercial Fisheries, Available from: http://www.dfw.state.or.us/mrp/docs/Backgrounder_Comm_Fishing.pdf (Accessed 31 August 2017)

Panteleev, G., M. Yaremchuk, V. Luchin, D. Nechaev, and T. Kukuchi (2012), Variability of the Bering Sea circulation in the period 1992–2010, *J Oceanogr*, *68*(4), 485–496, doi:10.1007/s10872-012-0113-0.

Paulson, C. A., and J. J. Simpson (1977), Irradiance Measurements in the Upper Ocean, *J. Phys. Oceanogr.*, *7*(6), 952–956, doi:10.1175/1520-0485(1977)007<0952:IMITUO>2.0.CO;2.

Pielke, R. A. (2007), *The Honest Broker: Making Sense of Science in Policy and Politics*, Cambridge University Press.

Reed, R. K., and P. J. Stabeno (1999), The Aleutian North Slope Current, in *Dynamics of the Bering Sea*, edited by T. R. Loughlin and K. Ohtani, pp. 177–191, University of Alaska Sea Grant, Fairbanks, Alaska.

Roden, G. I. (1995), Aleutian Basin of the Bering Sea: Thermohaline, oxygen, nutrient, and current structure in July 1993, *J. Geophys. Res.*, *100*(C7), 13539–13554, doi:10.1029/95JC01291.

Schmoldt, A., H. F. Benthe, and G. Haberland (1975), Digitoxin metabolism by rat liver microsomes, *Biochem. Pharmacol.*, *24*(17), 1639–1641.

Seacast (2017), Seacast, Available from: http://seacast.org/ (Accessed 31 August 2017)

Shchepetkin, A. F., and J. C. McWilliams (2003), A method for computing horizontal pressure-gradient force in an oceanic model with a nonaligned vertical coordinate, *J. Geophys. Res.*, *108*(C3), 3090, doi:10.1029/2001JC001047.

Shchepetkin, A. F., and J. C. McWilliams (2005), The regional oceanic modeling system (ROMS): a split-explicit, free-surface, topography-following-coordinate oceanic model, *Ocean Modelling*, *9*(4), 347–404, doi:10.1016/j.ocemod.2004.08.002.

Smithson, M. (2008), The many faces and masks of uncertainty, in *Uncertainty and Risk: Multidisciplinary Perspectives*, pp. 13–25.

Sohn, D., L. Ciannelli, and J. T. Duffy-Anderson (2010), Distribution and drift pathways of Greenland halibut (Reinhardtius hippoglossoides) during early life stages in the eastern Bering Sea and Aleutian Islands: Distribution and drift pathways of Greenland halibut, *Fisheries Oceanography*, *19*(5), 339–353, doi:10.1111/j.1365-2419.2010.00549.x.

Stabeno, P. J., D. J. Schumacher, and K. Ohtani (1999), The Physical oceanography of the Bering Sea, in *Dynamics of the Bering Sea*, edited by T. R. Loughlin and K. Ohtani, pp. 1–28, University of Alaska Sea Grant, Fairbanks, Alaska.

Stabeno, P. J., D. G. Kachel, N. B. Kachel, and M. E. Sullivan (2005), Observations from moorings in the Aleutian Passes: temperature, salinity and transport, *Fisheries Oceanography*, *14*, 39–54, doi:10.1111/j.1365-2419.2005.00362.x.

Stabeno, P. J., C. Ladd, and R. K. Reed (2009), Observations of the Aleutian North Slope Current, Bering Sea, 1996–2001, *J. Geophys. Res.*, *114*(C5), C05015, doi:10.1029/2007JC004705.

Star, S. L., and J. R. Griesemer (1989), Institutional Ecology, `Translations' and Boundary Objects: Amateurs and Professionals in Berkeley's Museum of Vertebrate Zoology, 1907-39, *Soc Stud Sci*, *19*(3), 387–420, doi:10.1177/030631289019003001.

Vestfals, C. D., L. Ciannelli, J. T. Duffy-Anderson, and C. Ladd (2014), Effects of seasonal and interannual variability in along-shelf and cross-shelf transport on groundfish recruitment in the eastern Bering Sea, *Deep Sea Research Part II: Topical Studies in Oceanography*, *109*, 190–203, doi:10.1016/j.dsr2.2013.09.026.

Walsh, J. E., W. L. Chapman, and D. H. Portis (2009), Arctic Cloud Fraction and Radiative Fluxes in Atmospheric Reanalyses, *J. Climate*, *22*(9), 2316–2334, doi:10.1175/2008JCLI2213.1.

Yu, P., A. L. Kurapov, G. D. Egbert, J. S. Allen, and P. M. Kosro (2012), Variational assimilation of HF radar surface currents in a coastal ocean model off Oregon, *Ocean Modelling*, *49–50*, 86–104, doi:10.1016/j.ocemod.2012.03.001.

Zhang, J., R. Woodgate, and R. Moritz (2010), Sea Ice Response to Atmospheric and Oceanic Forcing in the Bering Sea, *J. Phys. Oceanogr.*, *40*(8), 1729–1747, doi:10.1175/2010JPO4323.1.